Understanding the dependence of mean precipitation on convective treatment in tropical aquachannel experiments

Hyunju Jung[1], Peter Knippertz[1], Yvonne Ruckstuhl[2], Robert Redl[2], Tijana Janjic[2,3], and Corinna Hoose[1]

[1]Institute of Meteorology and Climate Research (IMK), Department Troposphere Research, Karlsruhe Institute of Technology (KIT), Karlsruhe, Germany
[2]Meteorological Institute, Ludwig Maximilian University of Munich, Munich, Germany
[3]Mathematical Institute for Machine Learning and Data Science, KU Eichstätt-Ingolstadt, Ingolstadt, Germany

Correspondence: Hyunju Jung (hyunju.jung@kit.edu)

Abstract. The intertropical convergence zone (ITCZ) is a key circulation and precipitation feature in the tropics. There has been a large spread in the representation of the ITCZ in global weather and climate models for a long time, the reasons for which remain unclear. This manuscript presents a novel approach with which we disentangle different physical processes responsible for the changeable behavior of the ITCZ in numerical models. The diagnostic tool is based on a conceptual framework devel-

5 oped by Emanuel (2019) and allows for physically consistent estimates of convective mass flux and precipitation efficiency for simulations with explicit and parameterized convection. We apply our diagnostics to a set of tropical aquachannel experiments using the ICOsahedral Nonhydrostatic (ICON) model with horizontal grid resolution of 13 km and with various representations of deep and shallow convection. The channel length corresponds to the Earth's circumference and has rigid walls at 30°N/S. Zonally symmetric sea surface temperatures are prescribed.

10   All four runs share overall similar rainfall patterns and dynamical structures. They simulate an ITCZ at the equator coinciding with the ascending branch of the Hadley circulation, descending branches at 15°N/S with subtropical jets and easterly trade wind belts straddling the ITCZ. Differences are largest between runs with and without parameterized deep convection. With explicit deep convection, rainfall in the ITCZ increases by 35 % and the Hadley circulation as well as surface winds become stronger. Our diagnostic framework reveals that boundary-layer quasi-equilibrium is a key to physically understanding those

15 differences. The stronger surface horizontal winds with explicit deep convection essentially enhance surface enthalpy fluxes and thus perturb quasi-equilibrium in the boundary layer. This is balanced by increasing convective downdraft mass flux that carries low moist static energy from the lower troposphere into the boundary layer. The downdraft strength is proportional to convective updraft mass flux, which is closely linked to rainfall, since – somewhat surprisingly – the convective treatment does not appear to influence precipitation efficiency significantly. Changes in radiative cooling are largely compensated by changes

20 in dry stability, leading to little impact on rainfall. The results highlight the utility of our diagnostics to pinpoint processes important for rainfall differences between models, suggesting applicability for global climate model intercomparison projects.

1 Introduction

Moist convection is of paramount importance in the tropics because it not only controls the distribution of water vapor, clouds
and rainfall, but also interacts with other processes in a wide range of scales from turbulence and microphysical processes via
radiation and surface fluxes to large-scale circulations such as the Hadley cells that consist the overturning circulation between
30°N/S with an ascending branch at the equator (Webster, 2020). One of the examples that illustrate the complexity of processes
associated with moist convection is the so-called Intertropical Convergence Zone (ITCZ) (Schneider et al., 2014). Over oceans,
the ITCZ is collocated with low-level convergence and upper-level divergence of the Hadley circulation accompanied by low-
level easterly trade winds on the flanks (Johnson et al., 1999; Schwendike et al., 2014). Thermodynamic contrasts between the
ocean and the air and surface winds modulate surface enthalpy fluxes, of which enhancement increases rainfall by transporting
moisture and heat from the ocean into the air (Raymond et al., 2006; Paccini et al., 2021). Cumulonimbus clouds as well
as clear-sky, moist columns in the tropics trap outgoing longwave radiation and the moist columns increase the shortwave
absorption, while the dry columns and shallow clouds in the subtropics enhance net longwave cooling compared to the tropics
(Bony et al., 2015; Lau et al., 2020). An important parameter to characterize atmospheric behavior in the tropics is precipitation
efficiency, the fraction of rain produced for a given amount of condensate. It has been shown that precipitation efficiency is
linked to the ratio of cirrus to deep convective clouds (Stephens, 2005). The area fraction of these two cloud types modulates
outgoing longwave radiation, which in turn controls the Earth's energy budget (Lindzen et al., 2001; Hartmann and Michelsen,
2002; Mauritsen and Stevens, 2015).

Climatologically, the location of the ITCZ is slightly shifted into the northern hemisphere (Webster, 2020). However, state-
of-the-art general circulation models (GCMs) still struggle to accurately represent many characteristics of the ITCZ including
the double-ITCZ problem leading to excessive rainfall in the southern hemisphere (Fiedler et al., 2020; Tian and Dong, 2020).
Even in an idealized aquaplanet configuration, which avoids complexities associated with the land-sea distribution and orogra-
phy, the spatial and temporal distributions of mean precipitation are sensitive to type of numerical model (Stevens and Bony,
2013; Rajendran et al., 2013; Landu et al., 2014; Benedict et al., 2017), vertical and horizontal resolution (Li et al., 2011;
Retsch et al., 2017, 2019) and representation of convection (Möbis and Stevens, 2012; Nolan et al., 2016; Retsch et al., 2019;
Rios-Berrios et al., 2022).

Most of the current weather and climate models employ parameterizations for shallow and deep convection. The former
plays an important role for the exchange between the BL and the free troposphere, particularly in relatively dry areas (Schlem-
mer et al., 2017; Naumann et al., 2019; Sakradzija et al., 2020), and the latter is key for rainfall generation and vertical energy
transport through latent heat release and mixing with ambient air (Emanuel et al., 1994b; Bechtold, 2017; Webster, 2020).
Explicitly representing convection on the model grid and thus avoiding convection parameterization is thought to be promis-
ing to reduce errors by permitting multi-scale interactions between convection and the large-scale circulation (Randall, 2013;
Palmer and Stevens, 2019; Tomassini, 2020), but it requires high model resolution. The appropriate horizontal grid spacing
is arguably $< 10\,\mathrm{km}$ (Weisman et al., 1997; Hong and Dudhia, 2012; Prein et al., 2015) with some extreme limit of $100\,\mathrm{m}$
(Kwon and Hong, 2017; Jeevanjee, 2017). Current global weather models use horizontal grid spacing of about $10\,\mathrm{km}$ (Becker

et al., 2021; Gehne et al., 2022). It is now feasible and affordable to conduct regional to global simulations with explicit deep convection (Satoh et al., 2017; Stevens et al., 2019; Schär et al., 2020; Wedi et al., 2020). These convection-permitting models show promising results, particularly in the tropics where baroclinic instability is of little relevance for weather systems. Explicit

60 convection captures the spatial and temporal variability of tropical rainfall more realistically compared to parameterized convection (Stevens et al., 2020). Wind-induced surface exchange of heat and moisture is also improved, as shown for the tropical Atlantic Ocean by Paccini et al. (2021). Moreover, explicit deep convection performs better in terms of convectively coupled equatorial waves (Judt and Rios-Berrios, 2021) and gravity wave momentum fluxes, which are often triggered by convection in the the tropics and subtropics (Stephan et al., 2019).

65 Despite these many improvements, models with explicit deep convection do not outperform those with parameterizations in every aspect. Parameterized deep convection is in better agreement with observations than explicit deep convection in terms of mean rainfall distribution (Wedi et al., 2020). Furthermore, Becker et al. (2021) demonstrated that their new convection parameterization scheme, which improves the coupling of convection to mesoscale dynamics, outperformed explicit deep convection in terms of both mean and intensity of rainfall over tropical Africa. Jung and Knippertz (2023) showed that the representation

70 of equatorial waves does not deviate much between explicit and parameterized deep convection when using a global forecast model. These results indicate that resolving convection does not automatically improve the multi-scale interactions in the atmosphere but that an accurate representation of physical processes and links between them are crucial.

A general problem in this context is that it is far from trivial to disentangle the reasons for the difference in performance when switching from parameterized to explicit deep convection, since convection couples and interacts with so many physical

75 processes. To tackle this problem, we here propose an innovative diagnostic tool based on a conceptual framework developed by Emanuel (2019). This framework is built around boundary-layer quasi-equilibrium (BLQE), the weak temperature gradient approximation, and mass and energy conservation. BLQE describes a balance of moist entropy in the subcloud layer. The balance is achieved between surface fluxes, which transport warm, moist air into the subcloud layer, and convective downdrafts and environmental subsidence, which transport cool, dry air from the free troposphere into the subcloud layer (Emanuel et al.,

80 1994a; Raymond, 1995). The weak temperature gradient approximation neglects horizontal temperature advection implying a balance between diabatic heating and vertical advection (Sobel et al., 2001). Emanuel (2019)'s framework considers processes on a time scale longer than that associated with the redistribution of energy by internal gravity waves. A key parameter of the conceptual model is the precipitation efficiency that summarizes the collective effects of turbulent and microphysical processes. Despite its relative simplicity, the framework is able to explain fundamental characteristics of the tropical atmosphere such as

85 the exponential relationship between rainfall and column relative humidity (Bretherton et al., 2004), convective self-aggregation (Bretherton et al., 2005) and the horizontal structures of the Walker and Hadley circulations. We refer to Emanuel (2019) for further demonstrations of atmospheric phenomena in his framework.

The goal of our study is to disentangle the physical processes contributing to differences in the ITCZ when changing the representation of deep and shallow convection in a numerical model. To avoid complexity associated with continents, orography,

90 zonal asymmetries and influences of the extratropics on the tropical conditions, we conducted a set of tropical aquachannel experiments with time-constant equator-symmetric sea surface temperatures (SSTs). The simulations are as realistic as pos-

sible by including a latitude-dependent Coriolis parameter and a diurnal cycle in solar irradiance. Section 2 explains further details of the model and experimental design. Section 3 describes the large-scale behavior of the aquachannel experiments and differences among four convective treatments. Section 4 presents our diagnostic approach based on Emanuel (2019). Results

95 from applying the new approach to the tropical aquachannel simulations are shown and discussed in Sect. 5. Conclusions are given in Sect. 6.

2   Method

2.1   Model

We use version 2.6.3 of the ICOsahedral Nonhydrostatic (ICON) model (Zängl et al., 2015) in the numerical weather predic-
100 tion (NWP) configuration. The model solves the fully compressible nonhydrostatic atmospheric equations of motion on an icosahedral-triangular Arakawa-C grid. Radiation is computed using the Rapid Radiative Transfer Model (RRTM) (Mlawer et al., 1997). A single-moment microphysical scheme is used to predict cloud water, rain water, cloud ice and snow (Seifert, 2008). A turbulent kinetic energy scheme is used for the representation of turbulent mixing and surface-to-atmopsphere transfer (Raschendorfer, 2001; Mellor and Yamada, 1982). Our model configuration closely follows the operational setup, including a
105 full non-linear Coriolis parameter, but some aspects are different for the specific purpose of our study. The surface of the entire model domain is covered by water (aquaplanet or aquachannel simulation) to exclude complexities associated with topography, and the diurnal cycle has fixed equinoctial insolation over the whole simulation period. Zonally symmetric SSTs are prescribed with a maximum of $27\,°C$ at the equator dropping to approximately $5\,°C$ at 60°N/S. This SST distribution has been used in other studies and is called the "Qobs" profile (Neale and Hoskins, 2000). There is no feedback of the atmosphere on the ocean
110 and the underlying water surface, effectively making the ocean an indefinite energy source.

2.2   Simulation setup

To spin up our aquachannel simulations, we adapt the modeling practice used in Bretherton and Khairoutdinov (2015). First we conduct a global aquaplanet simulation with a horizontal grid spacing of $40\,km$ and a time step of $300\,s$. The initialization of the $40\,km$ aquaplanet runs follows the Qobs case of Neale and Hoskins (2000). The number of vertical levels is 90 with
115 the model top at $75\,km$. Deep and shallow convection are parameterized using a bulk mass-flux scheme (Bechtold et al., 2008; Tiedtke, 1989). The $40\,km$ global aquaplanet experiment is run for 120 simulation days (gray solid bar in Fig. 1), after which the grid spacing is reduced to $26\,km$ with a time step of $225\,s$ and the simulation is continued for another 90 days. Finally, the model domain is restricted to a channel geometry between 30°N and 30°S and the horizontal grid spacing is reduced to $13\,km$ with a time step of $112.5\,s$ (black solid bar in Fig. 1). The domain encloses the entire globe and forms a closed ring in the zonal
120 direction. Walls closed by setting the meridional wind component to zero are introduced at the latitudinal boundaries where virtual potential temperature, water vapor mixing ratio, air density, and zonal and vertical winds are prescribed by zonally and temporally averaging them at 30°N and 30°S from the $26\,km$ aquaplanet simulation. The prescribed variables at the closed
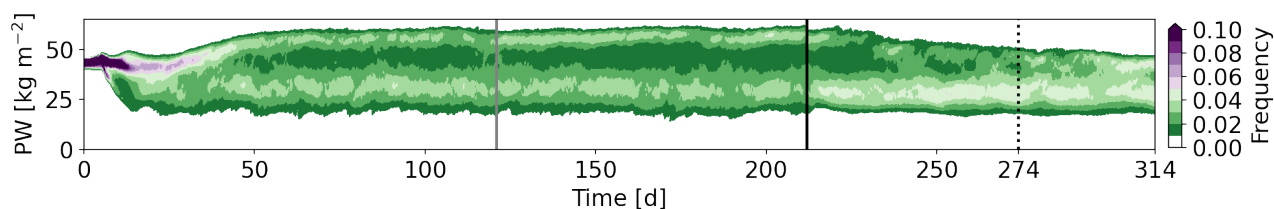
Figure 1. Evolution of the frequency density distribution of precipitable water in the equatorial belt between 20°N/S over a successive set of the aquaplanet and aquachannel simulations. The gray solid line indicates when the $26\,\mathrm{km}$ aquaplanet run begins, the black solid line when the $13\,\mathrm{km}$ aquachannel run begins and the dotted line marks when the analysis period of 40 days begins.

walls are time-invariant, zonally constant but vertically variant. Except for the aforementioned quantities, all other variables are set to zero at the walls. The setup for the aquachannel run is identical to the aquaplanet runs except for the simulation
125 geometry and the horizontal resolution. The coarser aquaplanet simulations thus serve to obtain the boundary conditions and to spin up the aquachannel run with reduced computational cost. The total simulation period of the $13\,\mathrm{km}$ aquachannel run is 102 days, consisting of spin-up at the beginning of 62 days and the analysis period of 40 days. The output time step is hourly. Output variables are remapped from the original triangular grid to a regular grid at $0.2°$ grid spacing.

To illustrate the modelling approach, Fig. 1 depicts the evolution of the probability density distribution of precipitable water
130 (PW) in the equatorial belt ($20\,°\mathrm{N/S}$) over the entire run time from day 0 to 314. In the beginning of the $40\,\mathrm{km}$ aquaplanet simulation, PW is distributed narrowly around $40\,\mathrm{kg\,m^{-2}}$ but by day 50 the distribution has widened with a broad dry maximum around $25\,\mathrm{kg\,m^{-2}}$ and a narrower secondary maximum near $55\,\mathrm{kg\,m^{-2}}$. After that, the bimodal shape remains stable, even when the grid spacing is reduced from $40\,\mathrm{km}$ to $26\,\mathrm{km}$ on day 120. The moist maximum corresponds to the actual ITCZ region, while the dry maximum represents the large area of subsidence in the cooler outer tropics with relatively few intermediate
135 values of PW in between. Such a rapid evolution into a stable bimodal structures was seen in other aquaplanet simulations with Coriolis force (e.g., Arnold and Randall, 2015; Khairoutdinov and Emanuel, 2018), as the large-scale circulation redistributes moisture from the relatively homogeneous initial conditions.

When the $13\,\mathrm{km}$ aquachannel experiment begins on day 210, a considerable change can be observed. The range of PW slowly decreases due to a reduction of the moist columns and an increase in the frequency of dry areas despite little change
140 in magnitude. This drift slows down but still continues into the investigation period after day 274, suggesting that a full equilibrium has not been reached yet. Towards the end of the simulation around day 314, there are some indications of a bimodal distribution again, yet much closer to each other than in the global simulation before day 210. The reason for this behavior lies in the prescribed properties at the closed walls. While in the global configuration, the Hadley cells span over 30°N/S, in the aquachannel configuration the model creates its own limited Hadley circulation away from the walls with subsidence around
145 15°N/S (discussed in detail in Sect. 3.2). The narrower overturning circulation reduces the amount of moisture converging into the ITCZ (not shown). It is also conceivable that the suppression of exchange with the higher latitudes reduces moisture uptake through surfaces fluxes triggered by dry intrusions from the midlatitudes (Bretherton and Khairoutdinov, 2015). Nonetheless,

the PW evolution over the entire simulation period exhibits smooth transitions not only from the coarse to high resolutions but also from the aquaplanet and aquachannel geometries.

150   Our original intention to prescribe zero meridional wind, and constant zonal and vertical winds from the 26 km aquaplanet experiment at the rigid walls was to simulate a Hadley circulation with descending branches near 30°N/S as in the global runs, but the model develops its own Hadley circulation rather than connecting its dynamical fields with the boundaries. We suspect that a possible reason is the suppression of eddy transport between the tropics and extratropics at the boundaries, forcing the model to develop its own subtropical jets internally. Ultimately, this also leads to distortions in the fields of cloud, radiation and

155 surface fluxes in the outer tropics. We presume that a wider channel or a two-way nested channel within a global domain would simulate jets at a more realistic location. However, the channel geometry suppresses tropical-extratropical interactions and thus reduces complexity. Furthermore, the advantage of having jets at more realistic location does not outweigh the merit of our configuration that is still able to reproduce a complex structure of dynamics and thermodynamics of the tropical atmosphere with affordable computational resource. To give as little weight as possible to the artifacts from the channel approach, we

160 restrict our analysis to an equatorial belt between 20°N/S (corresponds to area used in Fig. 1). We are confident that our analysis for this area can give useful insights into how convective treatment affects ITCZ processes, at least in a qualitative sense.

     We experimentally modify the representation of deep and shallow convection in the 13 km aquachannel configuration in the following way: (a) an experiment named P13 where the deterministic deep and shallow convection schemes are turned on

165 (already shown in the context of Fig. 1), (b) S13 where only the deep convection scheme is turned off, (c) SS13 where the standard deterministic shallow convection scheme (Bechtold et al., 2008; Tiedtke, 1989) is replaced by a stochastic scheme (Sakradzija et al., 2015, 2020), and (d) E13 where both deep and shallow convection schemes are turned off. The different convective treatments are summarized in Table 1. In the stochastic shallow convection scheme, the shallow-cloud ensemble is represented based on the theory of Craig and Cohen (2006). The number of new clouds is set using a Poisson distribution and

170 the lifetime average mass flux using a Weibull distribution. In the stochastic scheme there are two constraints: the mass flux closure of the deterministic scheme to constrain the ensemble average mass flux and the surface Bowen ratio to control the average mass flux per cloud (Sakradzija and Hohenegger, 2017). All aquachannel experiments share the same aquaplanet runs as spin-up. The different convective treatment is introduced when the channel geometry is introduced (black solid bar in Fig. 1 at day 210). Other than the different representations of convection, the setups remain identical among the 13 km aquachannel

175 experiments.

     In the following sections, we will analyse the last 40 days of each aquachannel experiment, i.e., after spin-up (day 274–314). For the remainder of the manuscript, the beginning of the analysis period is referred as to day 0, corresponding to the dotted bar in Fig. 1.

Table 1. Treatment of deep and shallow convection schemes for each experiment.

| Exp. name	Deep conv.	Shallow conv.
P13	On	On (deterministic)
S13	Off	On (deterministic)
SS13	Off	On (stochastic)
E13	Off	Off

3 Overview of aquachannel experiments

180 To illustrate the overall structure of our experiments, this section presents an analysis of precipitation and circulation features for the last 40 simulation days.

3.1 Precipitation

The latitudinal distributions of zonally and time averaged precipitation are shown in Fig. 2a for the four different convective treatments. All experiments present a distinct ITCZ region with high mean precipitation concentrating between 5°N/S, where

185 the SST maximum is prescribed. Explicit deep convection (S13, SS13 and E13) yields greater mean precipitation in the ITCZ than parameterized deep convection (P13) by about 35 %. (Between 5°N/S the time and zonally averaged precipitation is 7.28, 9.86, 9.73 and $9.84\,\mathrm{mm\,d^{-1}}$ for P13, S13, SS13 and E13, respectively.) P13 also produces a narrower, more pointy rainfall distribution. The treatment of shallow convection does not appear to have a large influence on the ITCZ structure. Outside of the ITCZ or the outer tropics, the overall rainfall amount and the differences between the experiments are relatively small.

190 Rainfall decreases to less than or equal to $1\,\mathrm{mm\,d^{-1}}$ at around 10°N/S and beyond this slightly increases with latitude. This pattern of rainfall in the outer tropics is also observed in other aquaplanet, aquachannel and aquapatch simulations (e.g., Nolan et al., 2016; Rios-Berrios et al., 2022). It is due to rainfall embedded in filaments of high PW being sheared off from the ITCZ into the outer tropics (see the Video Supplement).

The rainfall intensity distribution further underlines the substantial difference between explicit and parameterized deep

195 convection (Fig. 2b). Light and moderate rains ($< 30\,\mathrm{mm\,d^{-1}}$) occur more frequently in P13 than the others, which produce extreme rainfall rates of $400\,\mathrm{mm\,d^{-1}}$ and more, leading to the overall larger precipitation in the ITCZ. Correspondingly, the Video Supplement depicts that large-scale systems of precipitation with weak intensity are formed in P13, whereas intense, localized storms are formed in S13, SS13 and E13. The much higher intensities also lead to a more wiggly zonal average as shown in Fig. 2a. It is speculative that extreme rainfalls with explicit deep convection is due to underresolved convective

200 heating and mixing at $13\,\mathrm{km}$ grid spacing, generating strong updrafts and consequently extreme rainfall to remove instability in columns, which is somewhat in line with grid-point storms but rather found in convection parameterizations (Giorgi, 1991; Scinocca and McFarlane, 2004; Chan et al., 2014). This difference in rainfall intensity between parameterized versus explicit
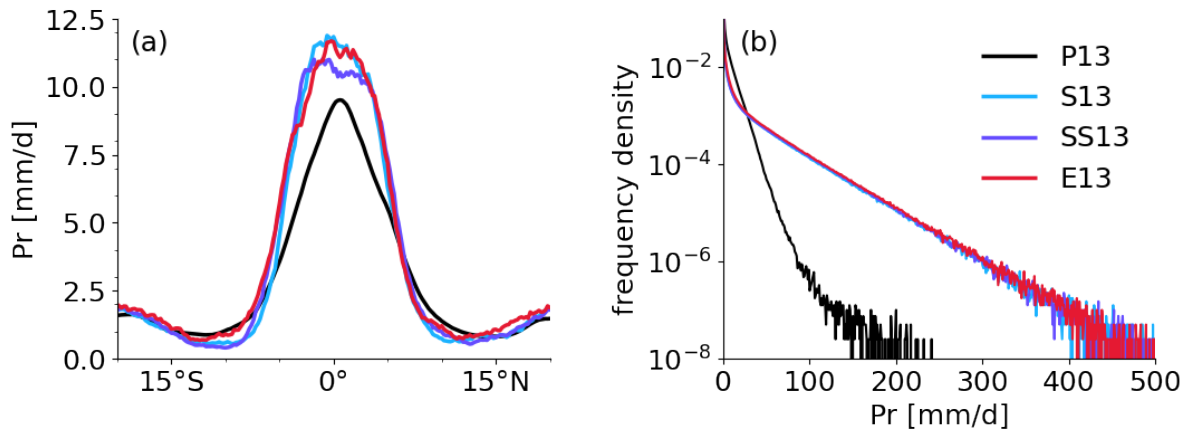
Figure 2. Distributions of (a) time and zonal mean of precipitation rate (Pr) and (b) precipitation intensity between 20°N/S. For the intensity distribution daily precipitation is grouped in model grids with the bin size of $1\,\mathrm{mm\,d^{-1}}$. Note the logarithmic vertical axis in (b).

deep convection was also observed in realistic simulations (Pante and Knippertz, 2019; Judt and Rios-Berrios, 2021; Becker et al., 2021).

3.2 Dynamical structure

Figure 3 shows a cross section of the time mean meridional-height mass stream function and zonal wind. The meridional-height mass stream function is calculated by integrating the meridional wind from the surface level to a certain altitude. Volumetric flux is conserved along a line of a constant meridional-height mass stream function. P13 features a largely equator-symmetric troposphere-deep Hadley circulation with low-level convergence and corresponding upper-level divergence in the ITCZ (Fig. 3a). The remaining small asymmetries, which occur despite the symmetric nature of our simulation setup, are a further indication that the simulations may not have fully reached equilibrium. The descending branches occur around 15°N/S, which is narrower than the climatological Hadley circulation in the real atmosphere (Webster, 2020) and in global aquaplanet simulations (not shown). The narrower Hadley circulation in the aquachannel experiments is because the exchange between the tropics and extratropics is suppressed at the closed walls of the tropical channel (discussed in Sect. 2.2). Strong westerly upper-tropospheric jets occur at the outer edges of these narrow Hadley cells reaching an averaged speed of $30\,\mathrm{m\,s^{-1}}$. These in principle resemble the subtropical jets of the real atmosphere but shifted closer to the equator and weaker. The low-level easterly trade wind belt starts at about 14°N/S and reaches about $2\,\mathrm{km}$, above which westerlies dominated. This creates a considerable westerly shear for the ITCZ convection (see the Video Supplement).

The other experiments (Fig. 3b–d) generally produce similar large-scale dynamical features as P13. However, the over-turning circulation and accompanying jets are strengthened. The maximum value of the mass stream function is 1.3×10^{11}, 1.81×10^{11}, 1.82×10^{11} and $1.84 \times 10^{11}\,\mathrm{kg\,s^{-1}}$ for P13, S13, SS13 and E13, respectively. This means that volumetric flux is greater with explicit deep convection, indicating stronger large-scale circulation. The strength of the simulated circulation is in
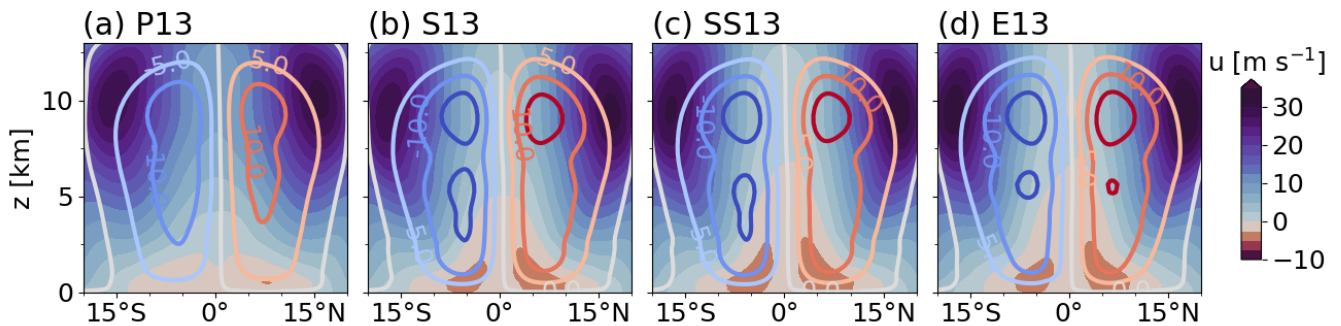
Figure 3. Time and zonal mean of zonal wind $[\mathrm{m\,s^{-1}}]$ (shading) and meridional-height mass stream function $[10^{10}\,\mathrm{kg\,s^{-1}}]$ (contour lines) for the analysis period in experiment (a) P13, (b) S13, (c) SS13 and (d) E13. The interval for the colored contours is $5 \times 10^{10}\,\mathrm{kg\,s^{-1}}$.

agreement with other aquaplanet studies (Medeiros et al., 2016; Rios-Berrios et al., 2020), but P13 is at the lower end of the range found in the other studies. The stronger large-scale circulation with explicit deep convection is accompanied by stronger

225   trade winds, with an increase of surface wind speed to about $4\,\mathrm{m\,s^{-1}}$. Such an increase of surface winds was also shown by a study using the ICON-NWP in a more realistic setup (Paccini et al., 2021). Furthermore, the runs with explicit deep convection exhibit equatorial easterlies in the middle troposphere up to 5–$7\,\mathrm{km}$, while P13 exhibits equatorial westerlies there. Possibly the explicit deep convection produces more upward convective momentum transport. This mechanism may also weaken the westerlies in the upper troposphere, leading to an overall much enhanced horizontal wind shear compared to E13. The vertical

230   shear in contrast is reduced in the ITCZ with potential consequences for the movement and organisation of convective systems (see the Video Supplement). There are some subtle differences in the strength and depth of the trade wind layer, supporting the idea that vertical momentum transport may play a role.

Another interesting aspect is that the runs with explicit deep convection (S13, SS13 and E13) generate a bimodal structure in the mass stream function, indicating a secondary shallow circulation that diverges polewards at around $7.5\,\mathrm{km}$ (Fig. 3b–d).

235   We speculate that this could be related to a better representation of the convective lifecycle comprising shallow, congestus and cumulonimbus clouds (Johnson et al., 1999; Khairoutdinov et al., 2009), which is not the case for P13 (not shown). Local temperature gradients due to stronger net cooling by congestus clouds in the vicinity of the ITCZ might create horizontal pressure gradients, which can in turn generate the secondary circulation. Furthermore, freezing and melting are substantial at around this level, which can be another source of local temperature gradients. As for P13, smaller hemispheric asymmetries

240   are evident in the mass stream function and zonal wind for S13, SS13 and E13, indicating remaining imbalances.

Overall, the analysis in this and the previous subsection reveals that physically consistent differences in precipitation amount and the large-scale circulation exist between explicit and parameterized deep convection with only smaller modulation by the treatment of shallow convection.

4 ITCZ diagnostics

245 This section presents our diagnostics based on Emanuel (2019)'s framework, which we will apply in Sect. 5 to output from the four aquachannel experiments to further explore the discussed differences in rainfall and large-scale circulation.

The framework of Emanuel (2019) assumes boundary-layer quasi-equilibrium (BLQE; Raymond, 1995), the weak temperature gradient approximation (Sobel et al., 2001) and energy and mass conservation, and neglects horizontal advection of moist static energy in the boundary layer (BL). Using these assumptions, the framework formulates convective updraft mass flux M_u

250 as follows:

$$M_u = \frac{1}{1 - \epsilon_p} \left(\frac{F_{\mathrm{h}}}{h_{\mathrm{b}} - h_{\mathrm{m}}} - \frac{\dot{Q}}{S} \right). \tag{1}$$

where M_u is convective upward mass flux of water vapor in $\mathrm{kg\,m^{-2}\,s^{-1}}$, ϵ_p precipitation efficiency, F_{h} surface enthalpy flux, $\dot{Q}$ the radiative cooling, h_{b} and h_{m} moist static energy of the BL and the free troposphere, respectively and S dry stability. Moist static energy is defined as $h = \phi + c_p T + L_v q_v - L_f q_i$ with ϕ being geopotential, c_p the specific heat heat at constant

255 pressure, T temperature, L_v the latent heat of vaporization, L_f the latent heat of freezing, q_v specific humidity and q_i specific ice content. Equation 1 demonstrates that the convective updraft mass flux increases with increasing surface enthalpy flux, with decreasing the vertical difference in moist static energy, with decreasing radiative cooling and with increasing dry static stability. The complete set of the conceptual framework for M_u (Emanuel, 2019) is included in Appendix A.

One important parameter of the framework is ϵ_p, which represents the fraction of all condensate that reaches the ground as

260 precipitation. Microphysical processes are not treated explicitly but formulated through one constant value of ϵ_p. Also, ϵ_p is used to parameterize convective downdraft mass flux M_d as a function of M_u in the following way: $M_d = (1 - \epsilon_p)M_u$. For $\epsilon_p = 1$, all condensate precipitates, such that there is no evaporation and thus no downdraft mass flux. For $\epsilon_p = 0$, all condensate eventually evaporates again such that downdraft and updraft mass fluxes balance.

For simplicity, Emanuel (2019) assumed that the average of the tropospheric $\dot{Q}$ can be approximated with the radiative

265 cooling at the top of the BL in order to couple the budget of h and the large-scale thermodynamic balance (see details in Appendix A). Raymond et al. (2015) suggested to use a lower tropospheric quasi-equilibrium instead of the entire tropospheric adjustment because when h_{b} increases from its equilibrium, the lower troposphere responds to the deviation on a convective time scale. We thus average h in the lower troposphere between 0.5 and $5\,\mathrm{km}$ to obtain a typical value h_{m}, and the same layer is considered for $\dot{Q}$, which is an averaged quantity, and S, which represents a slope of dry static energy. For computing h_{b}, we

270 average h from the lowest atmospheric level of $10\,\mathrm{m}$ to an approximate BL top of $500\,\mathrm{m}$. We tested alternatives for the BL in the range from 0.4 to $1.5\,\mathrm{km}$ and for the troposphere from 4 to $9.5\,\mathrm{km}$, and found the main findings to be rather insensitive to the exact choice of altitudes (not shown).

To relate this conceptual framework to our physical output, we need to find a relation between the modelled precipitation (either explicit or parameterized) to convective mass flux. We assume that precipitation rate Pr is directly proportional to M_u
275   and ϵ_p:

$$\mathrm{Pr} = \epsilon_p \, M_u \langle q_v \rangle \tag{2}$$

with $\langle q_v \rangle$ being the column specific humidity. The notation $\langle X \rangle$ indicates the mass-weighted column mean quantity, $\int \rho X \, dz / \int \rho \, dz$.

Using Eqs. 1 and 2, we have two unknowns, M_u and ϵ_p, because the other quantities can be readily obtained from the model output and can solve for them. In principle M_u could be calculated from w for each simulation, but vertical motions of explicit
280   and parameterized convection contain different processes. Parameterized convection assumes a profile of w through convective adjustment (Tiedtke, 1989), whereas explicit w is computed from the dynamical core. Therefore, comparing these two motions directly from the model output is a comparison of apples and oranges. The same principle applies to ϵ_p which is related to M_u. In our diagnostics, M_u and ϵ_p are not obtained directly from vertical motion but indirectly using other consistent quantities. Thus, results are physically consistent across the experiments with different convective treatments.

5 Application

285

Section 3 showed substantial differences in the mean state among the different convective treatments, mainly between parameterized and explicit deep convection. Section 4 presented a diagnostic tool to compare these differences in a fair manner. Here we apply the diagnostics to averaged fields over the last 40 simulation days, with a particular focus on mean rainfall. Given the zonal symmetry of our tropical channel, we will mostly consider zonal means. Figure 4 shows each quantity in Eq. 1 for the
290   four different convective treatments. In the following, we will discuss the different aspects of the conceptual model one after another: Surface fluxes (Sect. 5.1), vertical structure of moist static energy (Sect. 5.2), radiative cooling (Sect. 5.3), stability (Sect. 5.4), precipitation efficiency and convective mass flux (Sect. 5.5), and finally meridional advection in the BL (Sect. 5.6).

5.1 Surface enthalpy fluxes

The time and zonal mean of surface enthalpy fluxes is shown in Fig. 4a. P13 has F_h maxima in the trades and a local minimum
295   in the ITCZ (black line in Fig. 4a), similar to the situation over real-world tropical oceans but confined to a narrower latitudinal stretch. The other experiments with explicit deep convection (S13, SS13 and E13) share similar latitudinal distributions but F_h increases compared to P13, in particular between 10°N/S (by 20–25 %). Note that shallow convection is represented by the deterministic shallow convection scheme for S13, by the stochastic shallow convection scheme for SS13 and explicitly for E13 (Sect. 2.2). This indicates that the main difference in F_h is due to the treatment of deep convection rather than shallow
300   convection. This is consistent with the differences in Hadley circulation and thus surface winds discussed in Sect. 3.2. The difference between explicit and parameterized convection remains smaller outside of the subsidence region (about 15°N/S) than in the inner tropics. To investigate whether also thermodynamic effects play a role for these differences in surface enthalpy
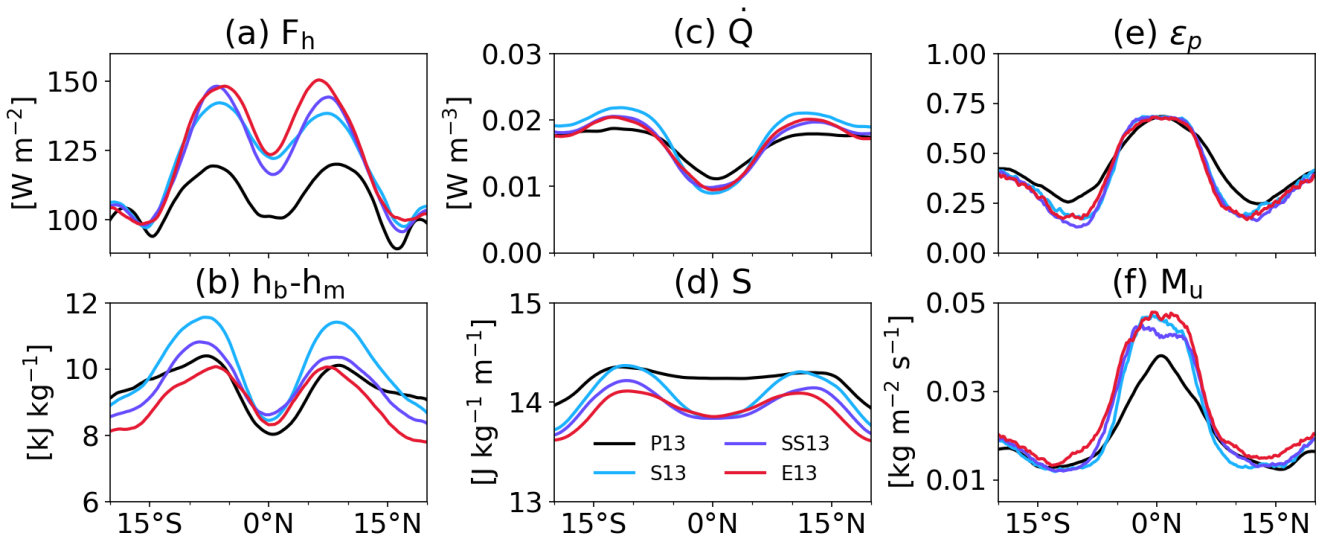
Figure 4. Time and zonal mean of (a) the surface enthalpy flux, (b) the vertical difference in moist static energy, (c) the lower tropospheric radiative cooling, (d) the dry static stability, (e) estimated precipitation efficiency and (f) estimated convective mass flux.

fluxes, we conduct a more detailed analysis. We decompose surface fluxes into their contributing factors (Sect. 5.1.1) and examine their statistical distribution (Sect. 5.1.2).

5.1.1 Decomposition of surface fluxes

In a standard air-sea bulk formula, surface enthalpy fluxes can be written as

$$F_{\mathrm{h}} = \rho_s L_v c_E \overline{U}_{\mathrm{h}} \Delta q + \rho_s c_p c_H \overline{U}_{\mathrm{h}} \Delta T \tag{3}$$

where ρ_s is the air density at the lowest model level, L_v is the latent heat of vaporization, c_p is the specific heat at constant pressure, c_E and c_H are the surface exchange coefficients for latent and sensible heat, respectively, $\overline{U}_{\mathrm{h}}$ is the surface horizontal wind speed, and Δq and ΔT are the air-sea moisture and temperature contrasts. For our analysis, we define $\Delta q = q_*(SST) - q_v(z_1)$ and $\Delta T = SST - T(z_1)$, where $q_*(SST)$ is the saturated specific humidity for a given SST and z_1 indicates the lowest model level of the atmosphere, which equals to $10\,\mathrm{m}$ in our case.

Figure 5a–c shows zonally and time averaged values of the individual terms of Eq. 3. The surface wind speed (Fig. 5a) mirrors the patterns in surface enthalpy fluxes (Fig. 4a) with maxima in the trade winds and with minima at the equator and in the area of the subsiding branches of the Hadley cells (Fig. 3). Winds then increase again further away from the equator. P13 shows considerably weaker surface winds by about $1\,\mathrm{m\,s}^{-1}$ than the other three runs out to about $10°$ from the equator, while
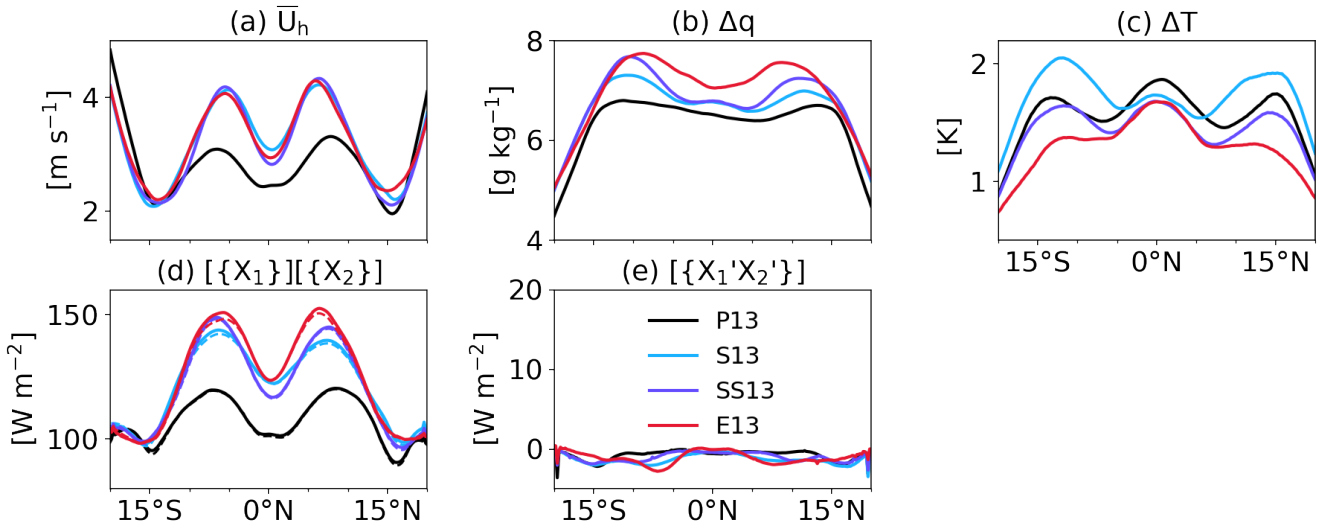
Figure 5. Time and zonal mean of surface properties: (a) the surface horizontal wind speed, (b) specific humidity contrast between the air and the ocean surface, and (c) temperature contrast between the air and the ocean surface. The bottom panels show contributions of (d) mean terms and (e) covariance terms (Eq. 4) to time and zonally averaged F_h. Here X represents the components of F_h such as $c_E \overline{U}_h$, $c_H \overline{U}_h$, Δq and ΔT. Dashed lines in (d) denote actual F_h from the model output (as in Fig. 4a) to facilitate the comparison.

the agreement in the rest of the domain is remarkably good. The treatment of shallow convection appears to have a rather small influence on surface winds.

The moisture contrast shows a much smoother latitudinal distribution and considerable contrasts between all four simulations

320 (Fig. 5b). In P13 Δq is almost constant around $6.60\,\mathrm{g\,kg^{-1}}$ within 15°N/S and then sharply falls off towards higher latitudes as q_* quickly drops at these latitudes. The explicit treatment of deep convection (S13, SS13 and E13) appears to allow for more vigorous downdrafts injecting dry air from the mid-troposphere into the BL. In contrast to other fields discussed so far, the treatment of shallow convection also plays a significant role. S13, which uses the same shallow convection scheme as P13 but no parameterization of deep convection, shows only slightly enhanced Δq, particularly in the trade wind zone, where shallow

325 mixing is important. The change to the stochastic treatment (SS13) from the deterministic treatment (S13) has little effect in the moist ITCZ area but further enhances Δq in the trades, eventually lining up with E13 at around 10°N/S.

Figure 5c shows that for ΔT the latitudinal structure and dependence on convective treatment is complex in contrast to the other two surface properties. All simulations have a local maximum at the equator, probably related to cool downdrafts from convection, but some have prominent maxima near the subsiding branches of the Hadley cells before all runs show a drop

330 off towards higher latitudes. E13 shows the overall smallest ΔT, possibly because it produces deeper convective downdrafts, leading to more adiabatic warming during the descent. The two simulations with parameterized shallow convection (S13 and

SS13) largely agree with E13 near the equator but show considerably larger ΔT in the outer tropics, in particular S13. The reasons for this are not entirely clear. Finally P13 has the highest ΔT at the equator and intermediate values in the outer tropics. However, these differences in ΔT have little impact on the surface enthalpy fluxes, since the surface sensible heat flux

335 contributes only about $10\,\%$ of the surface enthalpy fluxes. (In the latitudinal belt of 20°N/S the time and domain mean of the latent heat flux accounts for 97.4–$115.7\,\mathrm{W\,m^{-2}}$, while the surface sensible heat flux is 9.4–$11.3\,\mathrm{W\,m^{-2}}$.)

Surface enthalpy fluxes can be modulated by mean winds or thermodynamics and local perturbations of those components. To quantify this, the time and zonal mean of surface enthalpy fluxes (Fig. 4a) are separated into mean contribution and local perturbation contribution by surface horizontal wind speed and thermodynamic variables. Assuming X is a temporally and

340 spatially varying variable, we define $X = \{X\} + X'$ where $\{X\}$ indicates the horizontal mean (latitude and longitude) and X' the anomaly from the horizontal mean, and $X = [X] + X^*$ where $[X]$ indicates the time mean and X^* the anomaly from the time mean. If a field Y is a product of X_1 and X_2, i.e., $Y = X_1 X_2$, then $\{Y\} = \{X_1\}\{X_2\} + \{X_1' X_2'\}$ for the longitudinal mean (similarly for the time mean).

In the turbulence scheme used in ICON (Raschendorfer, 2001; Mellor and Yamada, 1982), the turbulent exchange coeffi-

345 cients are proportional to the turbulent kinetic energy and so we expect the coefficients to depend on surface wind speed (as well as vertical stability). This creates an overall more than linear dependence of the surface fluxes on wind speed. For simplicity, we combine the coefficients and surface wind speed together, i.e., $c_E\overline{U}_\mathrm{h}$ for the surface latent heat flux and $c_H\overline{U}_\mathrm{h}$ for the surface sensible heat flux. Here we derive turbulent exchange coefficients from the other variables in Eq. 3. For simplicity, we set the air density in Eq. 3 to a constant value of $1.2\,\mathrm{kg\,m^{-2}}$. Then, the surface latent and sensible heat fluxes vary with $c_E\overline{U}_\mathrm{h}$

350 and Δq, and $c_H\overline{U}_\mathrm{h}$ and ΔT, respectively. For example, a zonal mean of the surface latent heat flux can be expressed by the longitudinal mean and its fluctuation as $\{F_\mathrm{latent\,heat}\} = \rho_s L_v\{c_E\overline{U}_\mathrm{h}\}\{\Delta q\} + \rho_s L_v\{(c_E\overline{U}_\mathrm{h})'\Delta q'\}$. Thus, the zonal and time mean of F_h can be expressed as

$$
\begin{aligned}
[\{F_\mathrm{h}\}] ={}& \rho_s L_v\big[\{c_E\overline{U}_\mathrm{h}\}\big]\big[\{\Delta q\}\big] + \rho_s c_p\big[\{c_H\overline{U}_\mathrm{h}\}\big]\big[\{\Delta T\}\big] \\
&+ \rho_s L_v\big[\{(c_E\overline{U}_\mathrm{h})'\Delta q'\}\big] + \rho_s c_p\big[\{(c_H\overline{U}_\mathrm{h})'\Delta T'\}\big] \\
&+ \rho_s L_v\big[\{c_E\overline{U}_\mathrm{h}\}^*\{\Delta q\}^*\big] + \rho_s c_p\big[\{c_H\overline{U}_\mathrm{h}\}^*\{\Delta T\}^*\big].
\end{aligned}
\tag{4}
$$

The first and second terms on the right hand side in each row are from the surface latent and sensible heat fluxes, respectively.

355 In the first row $[\{X_1\}][\{X_2\}]$ indicates the contributions of time and zonally averaged surface wind speed combined with the turbulent coefficients and thermodynamic effects to the time and zonal mean of F_h (Fig. 4a). In the second row $[\{X_1' X_2'\}]$ indicates a product of local fluctuations which is averaged over time and longitude, i.e., the covariance which indicates the contributions of local perturbations. In the last row $[\{X_1\}^*\{X_2\}^*]$ indicates the time mean of a product of temporal fluctuations of spatial mean, which has near-zero values (not shown). Equation 4 represents fields that are averaged over longitude first,

360 and then time. Averaging, which is carried out over time and then longitude, is also tested (not shown) and does not change the results that are shown below.

Figure 5d shows latitudinal variations of contributions of the time-zonal mean values (the terms in the first row of Eq. 4). Overall, the contributions of the time-zonal mean values follow the patterns of the actual F_h (solid and dashed lines in Fig. 5d).

The differences between the contributions of the time-zonal mean values and the actual mean F_{h} are very small for P13 and
SS13, showing that the time-zonal mean components shape the mean F_{h}, whereas some departures are found in E13 and S13.

Figure 5e shows latitudinal variations of contributions of the covariance terms (the terms in the second row of Eq. 4) to
the time-zonal mean of F_{h}. Despite small magnitudes of the covariance terms compared to the mean contributions (Fig. 5d),
E13 and S13 exhibit negative contributions to the mean F_{h} in the trades. The negative contributions indicate that $(c_E \overline{\mathrm{U}}_{\mathrm{h}})' >$
0 coincides with $\Delta q' < 0$, meaning large q_v with a fixed q_* due to the prescribed SSTs, and vice versa for $(c_E \overline{\mathrm{U}}_{\mathrm{h}})' < 0$ and
$\Delta q' > 0$. Thus, the negative contribution can be interpreted as strong horizontal winds in a humid area or weak horizontal
winds in a dry area.

To summarize, the time-zonal mean of $c_E \overline{\mathrm{U}}_{\mathrm{h}}$ and Δq is the main contributor to shape the mean F_{h} for all experiments
(Fig. 5d), although for E13 and S13 the covariance terms have small negative contributions to F_{h} (Fig. 5e). The covariance
terms might not be small if the horizontal resolution is fine enough to resolve cold pools (Marsham et al., 2013). Lastly,
the temporal anomalies of the zonal mean components (the terms in the last row of Eq. 4) are very small compared to the
aforementioned components (not shown).

5.1.2 Statistical distribution

Previously, the latitudinal distributions of mean F_{h} were examined. We here construct statistical distributions of surface horizontal wind speed, thermodynamic disequilibrium and surface fluxes (Hsu et al., 2022) to provide a complementary view. This
does not require considering the turbulent exchange coefficients and allows us to examine how dependent surface fluxes are on
surface wind speed and thermodynamic disequilibrium. Specifically, we ignore the surface sensible heat flux, which accounts
for only about $10\,\%$ of surface enthalpy fluxes, and focus on the surface latent heat flux. Surface latent heat flux is grouped by
bins of $\overline{\mathrm{U}}_{\mathrm{h}}$ and Δq to outline distributions of the variables and the surface flux in one figure. We sample the surface latent heat
flux by bins of $\overline{\mathrm{U}}_{\mathrm{h}}$ and Δq at every output time step of one hour and at every grid point. The bin size for sampling is $1\,\mathrm{m\,s^{-1}}$
for $\overline{\mathrm{U}}_{\mathrm{h}}$ and $1\,\mathrm{g\,kg^{-1}}$ for Δq as in Hsu et al. (2022). We focus on the area between $10°$N/S where large differences in surface
enthalpy fluxes are observed (Fig. 4a). The results, however, do not change much when considering the area between $20°$N/S.

Figure 6 depicts a two-dimensional histogram of $\overline{\mathrm{U}}_{\mathrm{h}}$ and Δq, and corresponding values of the surface latent heat flux
(contour). For P13, the density distributions of both $\overline{\mathrm{U}}_{\mathrm{h}}$ and Δq are positively skewed with an extensively long tail for the
former (Fig. 6a). The bin of $\overline{\mathrm{U}}_{\mathrm{h}}$ of 1–$2\,\mathrm{m\,s^{-1}}$ and Δq of 6–$7\,\mathrm{g\,kg^{-1}}$ contains the maximum frequency density of $14.9\,\%$
(colored dot). Contour lines, which indicate corresponding surface latent heat flux, demonstrate that the surface latent heat
flux is more strongly dependent on $\overline{\mathrm{U}}_{\mathrm{h}}$ than on Δq. The maximum frequency density for $\overline{\mathrm{U}}_{\mathrm{h}}$ and Δq (colored dot) is located
between the surface latent heat contour lines of 50–$100\,\mathrm{W\,m^{-2}}$.

E13 (Fig. 6d) exhibits the largest contrast to P13, showing relatively evenly distributed $\overline{\mathrm{U}}_{\mathrm{h}}$ and Δq. The maximum density
(colored dot) accounts for $6.0\,\%$, which is less than a half of that for P13, and is in the bin of $\overline{\mathrm{U}}_{\mathrm{h}}$ of 3–$4\,\mathrm{m\,s^{-1}}$ and Δq of
7–$8\,\mathrm{g\,kg^{-1}}$, showing a greater surface wind and greater moisture contrast (seen also in Fig. 5a and b). The surface latent heat
flux (contour lines) increases strongly with increasing $\overline{\mathrm{U}}_{\mathrm{h}}$, while to lesser extent but noticeably it increases with increasing
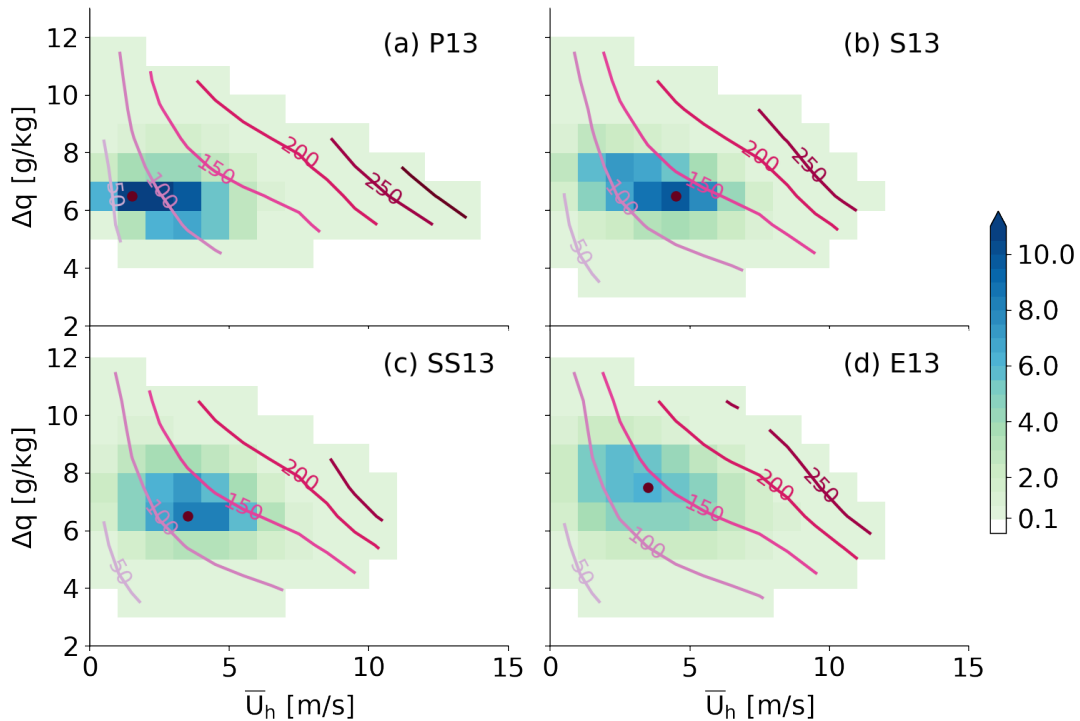
Figure 6. Two-dimensional histogram of surface wind speed and moisture contrast between the ocean and atmosphere in density (shading) with dots indicating the maxima. The minimum frequency density is 0.1 for shading. Contour lines indicate corresponding surface latent flux [$\mathrm{W\,m^{-2}}$] binned by the wind speed and moisture contrast. Contour interval is $50\,\mathrm{W\,m^{-2}}$ increasing from lighter to darker colors.

Δq. As expected from high F_h (Fig. 4a), the maximum density bin is located between the surface latent heat contour lines of 100–$150\,\mathrm{W\,m^{-2}}$.

The distributions of S13 and SS13 (Fig. 6b and c) are in closer agreement with E13 than P13. The maximum frequency

400   density (colored dot) lies between the contour lines of 100–$150\,\mathrm{W\,m^{-2}}$ consistent with small differences in F_h among the explicit deep convection runs (Fig. 4a). Additionally, the surface latent heat flux varies strongly with $\overline{\mathrm{U}}_\mathrm{h}$ and relatively weakly with Δq. The distributions are concentrated to the highest frequency density of $10\,\%$ for S13 and $8.4\,\%$ for SS13, showing some intermediate density distributions between P13 and E13.

In summary, Sect. 5.1.1 revealed that the time and zonal mean of $c_E\overline{\mathrm{U}}_\mathrm{h}$ and Δq mainly modulates the mean F_h and Sect. 5.1.2

405   showed that $\overline{\mathrm{U}}_\mathrm{h}$ is the dominant component for F_h distribution with the secondary role of Δq. These two different analyses demonstrate that mean $\overline{\mathrm{U}}_\mathrm{h}$ primarily modulates mean F_h.
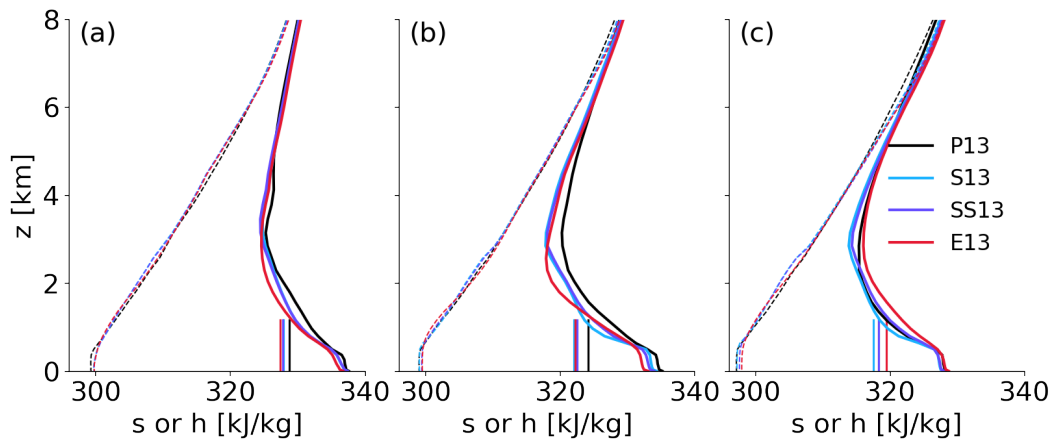
Figure 7. Profiles of the time and zonal mean of dry static energy (dashed) and moist static energy (solid) $[\mathrm{kJ\,kg^{-1}}]$ at (a) $0°$, (b) $8\,°\mathrm{N/S}$ and (c) $15\,°\mathrm{N/S}$. Those latitudes are chosen since they are representative of the ITCZ, the trade wind belt and the subsiding areas (see Sect. 3). The vertical bars represent the calculated h_m (average over 0.5 to $5\,\mathrm{km}$).

5.2 Vertical difference in moist static energy

Figure 4b shows the vertical difference in h between the BL and the lower troposphere described by $h_\mathrm{b} - h_\mathrm{m}$ (Eq. 1). This contrast is key for the BLQE, as it determines the reduction of h in the BL through convective downdrafts and large-scale

410   subsidence. Contrasts are smallest in the moist ITCZ region with relatively small differences among the four simulations with P13 showing the smallest values. Vertical h contrasts then increase markedly in the trade wind belt with much larger dependence on convective treatment, followed by a gradual fall-off towards higher latitudes. In the trade wind area, $h_\mathrm{b} - h_\mathrm{m}$ is smallest for E13 indicating deep mixing and conditions closer to moist neutrality. On the other hand, S13 shows much increased contrasts, suggesting that here deep mixing may be suppressed at the cost of more subtle shallow mixing. SS13 lies

415   in the middle between these two extremes. P13 shows a fundamentally different behavior with a much slower fall-off towards higher latitudes.

Profiles of h provide a deeper insight into the $h_\mathrm{b} - h_\mathrm{m}$ pattern. The solid lines in Fig 7 demonstrate h profiles below $8\,\mathrm{km}$ at characteristic latitudes for the ITCZ ($0°$), trades ($8°\mathrm{N/S}$) and subsidence areas ($15°\mathrm{N/S}$). Overall, h shifts to lower values from the equator to higher latitudes, following the prescribed SST pattern. The dashed lines in Fig. 7 show corresponding profiles

420   of dry static energy ($s = \phi + c_p T$) with hardly any difference between the experiments. Therefore, lower h with increasing latitude is largely equivalent to a drier air.

In the ITCZ (Fig. 7a), the BL is fairly shallow ($\sim 400\,\mathrm{m}$) and h_b differs little, changing by 0.1–$0.3\,\%$ (see Table 2). Note that the BL height is fixed for diagnostics to the layer of 10–$500\,\mathrm{m}$. This is higher than the ITCZ BL but does not impact the results. E13 shows the lowest value, possibly related to more frequent and or more intense convective downdrafts in line with more

425   intense rainfall (Fig. 2b). In the lower free troposphere, more distinct differences are evident, particularly between 1–$3\,\mathrm{km}$. E13

Table 2. Time and zonal average of moist static energy [$\mathrm{kJ\,kg^{-1}}$] and dry stability [$\mathrm{J\,kg^{-1}\,m^{-1}}$] at three different latitudes. The layer of 10–500 m and 0.5–5 km are used for the quantities in the BL h_b and in the lower troposphere h_m and dry stability S, respectively.

lat (°)	run	h_b	h_m	$h_\mathrm{b} - h_\mathrm{m}$	S
	P13	336.78	328.72	8.06	14.24
	S13	336.34	327.88	8.45	13.85
0	SS13	336.37	327.75	8.62	13.84
	E13	335.70	327.37	8.32	13.86
	P13	334.35	324.12	10.23	14.29
	S13	333.52	322.05	11.48	14.25
8	SS13	333.06	322.48	10.58	14.08
	E13	332.16	322.16	10.00	14.07
	P13	327.81	318.31	9.51	14.27
	S13	327.27	317.51	9.76	14.17
15	SS13	327.34	318.22	9.12	14.06
	E13	327.96	319.42	8.54	13.92

has again the overall lowest values, such that downdrafts can more effectively reduce h_b. Retsch et al. (2019) also found a drier lower troposphere for their explicit deep convection cases than for parameterized ones. S13 and SS13 show enhanced values relative to E13 around 2 km, while P13 has higher h throughout most of the layer up to 5 km. Applying a vertical average over 0.5 to 5 km, we obtain h_m, which varies between 327.4 and 328.7 $\mathrm{kJ\,kg^{-1}}$ (Table 2). Given that differences within and above

430 the BL are largely consistent between the runs, $h_\mathrm{b} - h_\mathrm{m}$ in the ITCZ increases by 3–6 % from P13 to S13, SS13 and E13 as also evident from Fig. 4b.

In the trade wind belt, differences among the four experiments in $h_\mathrm{b} - h_\mathrm{m}$ are larger than in the ITCZ (Figure 4b). This corresponds with more marked differences in the vertical profiles of h (Fig. 7b). The profiles are shifted to lower h from the ITCZ to the trade wind belt. Overall the shift is more evident for the explicit deep convection runs (S13, SS13 and E13)

435 than P13 which shows a moderate h decrease in the trade wind belt. The variations of h_b among the four experiments are systematic with decreasing from P13 to S13 or SS13 to E13 by 0.83–1.36 $\mathrm{kJ\,kg^{-1}}$ (see Table 2). Also, E13 has a higher BL height by around 100 m or one model level than P13. Meanwhile, h_m varies small among the explicit deep convection runs (S13, SS13 and E13; colored vertical bars in Fig. 7b) but largely decreases from P13 to any run with explicit deep convection by 1.64–2.07 $\mathrm{kJ\,kg^{-1}}$ (Table. 2). Yet, the profiles among the explicit deep convection runs in the lower troposphere do not

440 show a perfect match but rather subtle differences. SS13 exhibits somewhat an intermediate behavior of h between S13 and E13, such that SS13 alternates the patterns of h similar to S13 in the BL, E13 between 0.5–1.5 km and again S13 above 1.5 km. This intermediate behavior indicates that the stochastic scheme for shallow convection (SS13) mixes the air between the BL and lower troposphere more efficiently than the deterministic version (S13) but not as deeply as the explicit one (E13).

Consequently, this results in some unsystematic behavior of $h_{\mathrm{b}} - h_{\mathrm{m}}$ from one to another with E13 showing the lowest value,
445   then P13 and SS13 and finally with S13 showing the highest value (Fig. 4b).

In the subsidence region (Fig. 7c), the BL height is $500\,\mathrm{m}$ in all four experiments and h_{b} is fairly similar among the runs where E13 shows the largest value unlike the other latitudinal regions. The maximum difference between two runs in h_{b} is $0.69\,\mathrm{kJ\,kg^{-1}}$ (Table. 2). Also, E13 shows the largest value of h_{m}, indicating more moisture columns than the others as profiles for dry static stability show no substantial differences. This is the opposite of the results by Retsch et al. (2019) who showed
450   that the lower troposphere in the subsidence region is drier with explicit deep convection than parameterized deep convection. Given that the strength of the Hadley circulation is largely consistent with explicit deep convection (discussed in Sect. 3.2), lower-tropospheric moisture is presumably dominated by local mixing rather than large-scale subsidence effects. Likewise, local mixing between S13 and SS13 fundamentally differs in that vertical mixing, mainly in the lower atmospheric layer, is more efficient for the stochastic version (SS13) (Sakradzija et al., 2020). Accordingly, h_{m} for SS13 increases from S13 by
455   more than $0.5\,\mathrm{kJ\,kg^{-1}}$, which is less than $0.5\,\mathrm{kJ\,kg^{-1}}$ in other latitudinal regions (Table. 2). Thus, we see a systematic change of $h_{\mathrm{b}} - h_{\mathrm{m}}$ in the subsidence region, representing some effects of local mixing.

In summary, h_{b} and h_{m} in the ITCZ and the trade wind belt show some systematic changes from parameterized to explicit deep convection but the resulting pattern of $h_{\mathrm{b}} - h_{\mathrm{m}}$ varies with different convective treatments. The impact of shallow convective treatment is evident in profiles of h, particularly in the trade wind belt. The stochastic version of shallow convection
460   (SS13) exhibits the intermediate behavior of h between the deterministic version (S13) and explicit version (E13), consequently reflected on the latitudinal distribution of $h_{\mathrm{b}} - h_{\mathrm{m}}$ (Fig. 4b).

5.3 Radiative cooling

Figure 4c shows the time and zonal mean of radiative cooling in the lower troposphere (0.5–5 km). P13 exhibits the overall flattest latitudinal distribution with a minimum radiative cooling in the ITCZ and larger cooling in the outer tropics (Fig. 4c).
465   S13, SS13 and E13 show a similar pattern but less cooling in the ITCZ and stronger cooling in the outer tropics, the latter particularly true for S13. In the following, we will discuss this result in the context of total cloud cover (Fig. 8) and the latitudinal-height distribution of the radiative temperature tendency (Fig. 9).

Figure 8 shows that amongst all runs, P13 has the overall smallest cloud cover, peaking at about $80\,\%$ at the equator and falling off gradually to $37\,\%$ at 15°N/S beyond which there is a slight increase again. Consequently, radiative cooling in the
470   troposphere shows a marked contrast between the ITCZ region and the outer tropics (Fig. 9a). In the former, radiative cooling is generally reduced and there is even a slight warming below the tropopause, likely related to longwave absorption by optically thick cirrus (Senf et al., 2020). This is consistent with the fact that for P13 cloud ice in the upper troposphere is spread over a deeper layer by $1\,\mathrm{km}$ than in the other experiments (not shown). Note that the near-tropopause warming is not included in $\dot{Q}$ (Fig. 4c), which is averaged over $0.5\text{–}5\,\mathrm{km}$ (Sect. 4). In the outer tropics, radiative cooling increases and is quite homogeneous
475   across most of the free troposphere decreasing gently above about $9\,\mathrm{km}$ (Fig. 9a). The top of the BL stands out as an area of enhanced cooling associated with longwave emission from the top of shallow clouds into the relatively dry free troposphere above it.
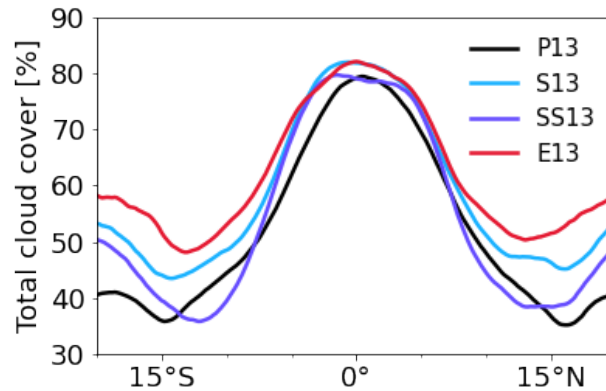
Figure 8. As in Fig. 4c but for total cloud cover.

The cloud cover and the radiative cooling in E13 show the largest contrast to P13. The cloud cover increases from P13 to E13 by $6\,\%$ in the ITCZ and by $34\,\%$ in the outer tropics (Fig. 8). Correspondingly, there are some differences in pattern of radiative cooling (Fig. 9d). Overall radiative cooling above the BL weakens due to increased vertical mixing around BL top by explicit deep and shallow convection. In the ITCZ, E13 exhibits only net radiative cooling, whereas P13 shows radiative warming near the tropopause. Longwave cooling is stronger when deep convection is explicitly represented because explicit deep convection releases more latent heat through microphysical processes than parameterized deep convection (can be inferred from more frequent extreme rainfall in explicit deep convection in Fig. 2b), which increases temperature of the atmospheric columns and consequently emits more longwave radiation. In the outer tropics, where the total cloud cover substantially increases from P13 to E13, radiative cooling in E13 shows signatures of shallow and congestus convection (Fig. 9d), which is hardly seen in the mean radiative cooling in P13 (Fig. 9a). The delicate structure demonstrates that E13 is able to construct a trimodal structure of deep, congestus and shallow clouds (Johnson et al., 1999; Khairoutdinov et al., 2009), consistent with the relatively high cloud cover. The weak BL radiative cooling reduces $\dot{Q}$ in the ITCZ and the mid-level clouds increase $\dot{Q}$ in the outer tropics from P13 to E13 (Fig. 4c).

S13 exhibits similar features to E13 in terms of cloud cover and radiative cooling (including $\dot{Q}$) in the ITCZ, but there are marked differences in the outer tropics. Cloud cover in S13 ($47.7\,\%$) is intermediate between P13 ($39.8\,\%$) and E13 ($53.2\,\%$) (Fig. 8). While the free-tropospheric cooling by radiation is consistent with E13, S13 (Fig. 9b) reveals that radiative cooling above the BL is substantially enhanced and very concentrated, creating a gap in cooling above that. This leads to the largest $\dot{Q}$ of all runs in the outer tropics (Fig. 4c).

Surprisingly, SS13 shows the closest cloud cover to P13 amongst all runs with explicit deep convection (Fig. 8). Free-tropospheric radiative cooling remains similar to S13 and E13, but the BL top cooling in the outer tropics is much reduced with slight enhancement at around $3\,\mathrm{km}$ (Fig. 9c). This is due to the fact that the stochastic version (SS13) allows for efficient mixing between the BL and the lower troposphere and for efficient BL convective heating (Sakradzija et al., 2020; Senf et al.,
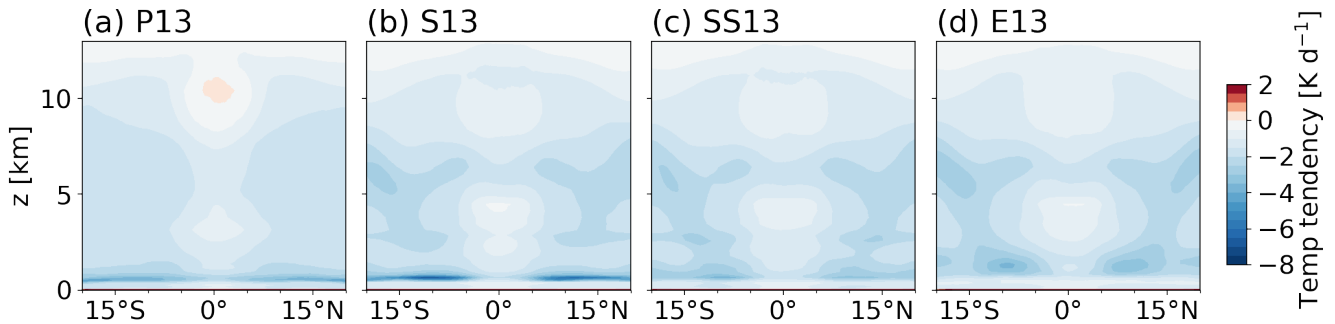
Figure 9. As in Fig. 3 but for net radiative temperature tendency.

2020). Consequently, this leads to overall similar $\dot{Q}$ to E13 (Fig. 4c), despite the very different vertical structures of radiative temperature tendency.

5.4 Dry stability

In the conceptual framework, the effects of radiative cooling need to be considered relative to the dry stability S (Eq. 1), which is shown in Fig. 4d. For P13, S is almost constant between 15°N/S with a value of $14.2\,\mathrm{J\,kg^{-1}\,m^{-1}}$ beyond which it drops slightly. The other experiments exhibit some noteworthy differences. In the ITCZ, explicit deep convection appears to create a somewhat lower stability by about $0.4\,\mathrm{J\,kg^{-1}\,m^{-1}}$ compared to P13 (Table 2). This may be related to the fact that parameterized convection is triggered a little more easily and can therefore more effectively stabilize the atmosphere in a convectively active region. This subtle difference is also evident from Fig. 7a. (The slope of s in the lower troposphere represents S.) In the outer tropics, the treatment of shallow convection has some effect on S, increasing S by about $0.1\,\mathrm{J\,kg^{-1}\,m^{-1}}$ from one experiment to another (Table 2): E13 likely produces the least shallow mixing and is thus least stable, followed by SS13 and S13. Finally, the largest stability is found in P13 to which both parameterized shallow and deep convection contribute. As in the ITCZ, differences are overall subtle and evident from profiles of s (Fig. 7b and c).

In the conceptual model the ratio of radiative cooling in the lower troposphere $\dot{Q}$ and dry stability S are regarded (second term in Eq. 1). As radiation and stability in all four runs largely compensate each other, the ratio is almost identical and also relatively constant over latitudes, accounting for $1.2\pm0.2\,\mathrm{g\,m^{-2}\,s^{-1}}$. In contrast, the effect of surface enthalpy fluxes and vertical contrast of h (first term in Eq. 1) accounts for 11.3–$13.7\,\mathrm{g\,m^{-2}\,s^{-1}}$ with standard deviation of 1.4–$1.6\,\mathrm{g\,m^{-2}\,s^{-1}}$. This demonstrates that despite all the details discussed above, the overall effect of radiation and stability to drive differences among the four simulations is minor.

5.5 Convective updraft mass flux and precipitation efficiency

Up to this point, we have examined the distributions of each term on the right-hand side in Eq. 1. To close our diagnostics, here we discuss M_u, ϵ_p and $\langle q_v \rangle$ which are directly related to rainfall (Eq. 2), and then link this discussion to the entire

Table 3. The averaged precipitation rate (Pr), column specific humidity ($\langle q_v \rangle$), convective updraft mass flux (M_u), precipitation efficiency (ϵ_p), surface enthalpy flux (F_h) and BL merdional advection (Adv) between 5°N/S for each experiment. The quantities in parentheses indicate those when the BL meridional advection is included (Eq. 5).

	Pr [mm d^{-1}]	$\langle q_v \rangle$ [g kg^{-1}]	M_u [kg m^{-2} s^{-1}]	ϵ_p	F_h [W m^{-2}]	Adv [W m^{-2}]
P13	7.28	4.0	0.0320 (0.0315)	0.629 (0.639)	105.6	4.4
S13	9.86	3.91	0.0416 (0.0391)	0.648 (0.692)	129.3	22.8
SS13	9.73	3.92	0.0412 (0.0387)	0.648 (0.691)	127.0	22.7
E13	9.84	3.74	0.0439 (0.0406)	0.639 (0.693)	134.9	29.3

framework. We start with those quantities in the ITCZ. Figure 4e shows that ϵ_p has the maxima there with almost constant values of 0.629–0.648 in all four experiments (Table. 3). Meanwhile, $\langle q_v \rangle$ marginally decreases from P13 to S13 and SS13 to E13 by around 2–6 % (Table. 3), indicating that P13 has the moistest atmospheric column in the ITCZ, as also seen in profiles

525 of h (Fig. 7a). Given the almost identical ϵ_p and the decreasing $\langle q_v \rangle$ from parameterized to explicit convection, M_u must increase from parameterized (P13) to explicit deep convection (S13, SS13 and E13) to increase rainfall accordingly (Eq. 2). Correspondingly, M_u increases from P13 to E13 by 37.2 % (Fig. 4f and Table. 3). A similar increase in M_u by about 29 % is shown for S13 and SS13. These differences in M_u are similar to those in Pr (33.7–35.2 %).

In the outer tropics, ϵ_p sharply decreases from the ITCZ with a minimum at around 9–12°N/S and beyond this increases

530 with latitude (Fig. 4e). The differences among the runs are substantial in the outer tropics, with ϵ_p varying between 0.214–0.306 (highest in P13). Mean values of $\langle q_v \rangle$ slightly vary with P13 marking the greatest value of 2.77 g kg^{-1} and with S13 marking the smallest value of 2.51 g kg^{-1} (not shown). From the ITCZ to the outer tropics M_u sharply decreases to about 0.015 kg m^{-2} s^{-1} (with E13 showing the upper limit of the range) and beyond the minimum slightly increases with latitude (Fig. 4f). These patterns of the minimum and marginal increase in ϵ_p and M_u are also observed in Pr (Fig. 2a), yet the

535 differences in Pr in the outer tropics among the runs do not vary as much as those in ϵ_p due to low ϵ_p, low M_u and low $\langle q_v \rangle$ there.

To summarize, we show that in the ITCZ, M_u substantially increases from parameterized (P13) to explicit deep convection (S13, SS13 and E13), while ϵ_p is almost identical among them and $\langle q_v \rangle$ marginally decreases from P13 to S13 and SS13 to E13. Surprisingly, the increase in Pr is not associated with ϵ_p but M_u. In radiative convective equilibrium (RCE), where the

540 large-scale circulation is absent, ϵ_p would be strongly linked to rainfall (Emanuel, 2019). Intuitively, an increase in rainfall would be strongly related to increasing precipitation efficiency (Narsey et al., 2019; Muller and Takayabu, 2020) but this is not the case in our simulations.

When revisiting all input variables in Eq. 1 for our diagnostics (Fig. 4), it is evident that in the ITCZ, F_h exhibits the same increasing tendency as M_u, while $h_b - h_m$ shows small differences. Meanwhile, $\dot{Q}$ and S compensate each other (Sect. 5.4),

545 which consequently have almost no effect on M_u. Therefore, M_u and F_h are strongly related to each other, which is explained by BLQE. Given constant ϵ_p in the ITCZ, an increase in M_u increases M_d, through $M_u = (1 - \epsilon_p)M_u$, which carries low h

from the lower troposphere into the BL to balance enhanced F_h. The change in F_h is associated with changing $\overline{\mathrm{U}}_\mathrm{h}$ (Sect. 5.1) which is closely linked to the Hadley circulation (Sect. 3.2). Thus, a different convective treatment changes a large-scale circulation and surface horizontal wind, which alters associated surface fluxes that are in balance with convective mass flux,
550 which is directly related to rainfall.

In the outer tropics, differences in ϵ_p (Fig. 4e) become evident between P13 and the other explicit deep convection runs (S13, SS13 and E13). However, Pr (Fig. 2a) is relatively small and does not vary much between the runs because of low absolute values of ϵ_p as well as the sharp decreases in M_u and $\langle q_v \rangle$ from the ITCZ. Beyond about 9–12°N/S, ϵ_p increases with increasing latitude, which is related to increasing Pr with latitude there. Nonetheless, differences in Pr remain small in the outer tropics
555 compared to the ITCZ due to small absolute values of related terms (ϵ_p, M_u and $\langle q_v \rangle$; see Eq. 2).

5.6   Meridional advection

Equation 1 is obtained by neglecting the horizontal advection in the BL. Here we test the sensitivity of the diagnostics when the advection term is included. A scale analysis for h budget of the BL (Eq. A3) reveals that the BL radiative cooling term can safely be ignored while the advection term is not fully negligible ($\mathrm{d}\dot{Q}_b \sim 1\,\mathrm{W\,m^{-2}}$, $\mathrm{d}\rho \boldsymbol{V}_h \cdot \nabla h \sim 10\,\mathrm{W\,m^{-2}}$, $F_\mathrm{h} \sim 100\,\mathrm{W\,m^{-2}}$).
560 With this, Eq. 1 can be expressed as:

$$M_u = \frac{1}{1-\epsilon_p}\Big(\frac{F_\mathrm{h}-\mathrm{d}\rho\boldsymbol{V}_h \cdot \nabla h}{h_\mathrm{b}-h_\mathrm{m}} - \frac{\dot{Q}}{S}\Big). \tag{5}$$

where d is the BL height and $\boldsymbol{V}_h$ is the horizontal velocity. Here, only meridional advection is taken into account because BL meridional and zonal gradients are in the order of 10 and $0.1\,\mathrm{J\,kg^{-1}\,km^{-1}}$, respectively, while BL meridional and zonal winds are comparable in magnitude. The advection term is calculated by integrating the meridional advection of h from the lowest
565 atmospheric layer at $10\,\mathrm{m}$ to the BL top at $500\,\mathrm{m}$, and assuming an air density of $1.2\,\mathrm{kg\,m^{-2}}$.

Figure 10 shows the latitudinal distribution of BL meridional advection and the impact of including it on precipitation efficiency and convective updraft mass flux. P13 shows near-zero values at the equator that increases away from the equator, leading to an average of $4.4\,\mathrm{W\,m^{-2}}$ in the ITCZ (Table 3). The small advection term in the ITCZ decreases M_u by $0.0005\,\mathrm{kg\,m^{-2}\,s^{-1}}$ and increases ϵ_p by 0.01 compared to the advection-free diagnostics (Sect. 5.5). At about 10°N/S, BL
570 meridional advection reaches the maximum of $13.4\,\mathrm{W\,m^{-2}}$ and beyond that decreases with increasing latitude, leading to an increase in ϵ_p by 0.022 and an decrease in M_u by $0.001\,\mathrm{kg\,m^{-2}\,s^{-1}}$ which are considerably small.

In contrast to P13, E13 exhibits a large contribution of BL meridional advection (Fig. 10a). The averaged advection in the ITCZ is $29.3\,\mathrm{W\,m^{-2}}$, consequently reducing M_u by $0.0033\,\mathrm{kg\,m^{-2}\,s^{-1}}$ but increasing ϵ_p by 0.054 (Table 3). At around 7°N/S the advection term shows local maxima of $33.8\,\mathrm{W\,m^{-2}}$ and then sharply decreases with increasing latitude. The overall large
575 meridional advection term for E13 is consistent with intensified $\overline{\mathrm{U}}_\mathrm{h}$ (Fig. 5a) and greater h shift in the BL with latitude (Fig. 7). Consequently, M_u marginally decreases by $0.0024\,\mathrm{kg\,m^{-2}\,s^{-1}}$ and ϵ_p increases by 0.037 in the outer tropics.

Similarly, SS13 shows large BL meridional advection in the ITCZ and has local maxima at around 7°N/S but overall weaker advection by around $6\,\mathrm{W\,m^{-2}}$ than E13 (Fig. 10a). The advection consideration leads to a decrease in M_u by $0.0025\,\mathrm{kg\,m^{-2}\,s^{-1}}$
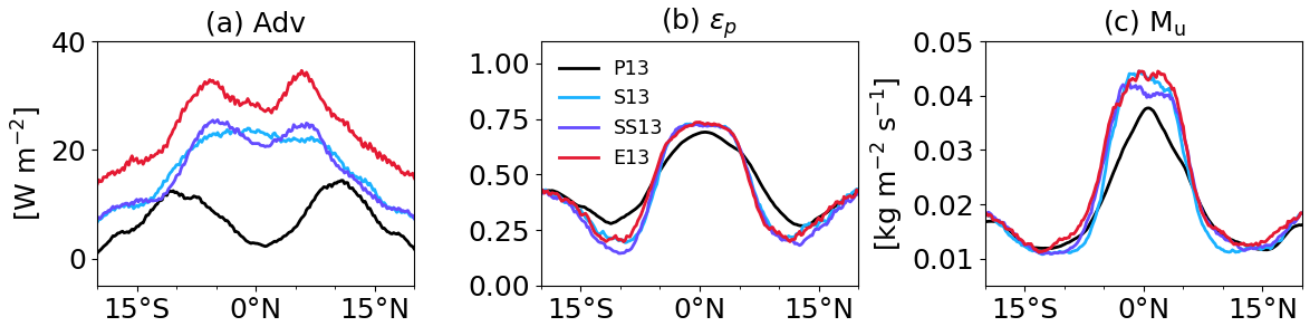
Figure 10. Time and zonal mean of (a) the meridional advection term $(\mathrm{d}\,\rho \boldsymbol{V}_h \cdot \nabla h)$, (b) estimated precipitation efficiency and (c) estimated convective mass flux using Eqs. 2 and 5.

and an increase in ϵ_p by 0.043 in the ITCZ (Table 3), which changes less strongly in the outer tropics (Fig. 10b and c). For

580   S13 meridional advection closely follows that for SS13 (Fig. 10a), leading to averaged advection of $22.8\,\mathrm{W\,m^{-2}}$ in the ITCZ (Table. 3). However, the maximum value is located in the ITCZ rather than at around 7°N/S. The minor increase from SS13 to S13 in $\overline{\mathrm{U}}_h$ in the ITCZ (Fig. 5a) and the slightly reduced meridional h gradient for S13 (Fig. 7a and b) lead to the different shapes between S13 and SS13. Despite this difference, M_u and ϵ_p in S13 and SS13 change by the almost same degree when considering meridional advection.

585   In summary, the meridional advection inclusion slightly increases ϵ_p and slightly decreases M_u for all four cases. The former in the ITCZ increases by $8\,\%$ from P13 to the other explicit deep convection runs (S13, SS13 and E13), which was almost identical without considering the advection term (Sect. 5.5). However, the close association between M_u and rainfall remains strong, showing that the increase in M_u from P13 is by 22.9–$28.9\,\%$, which contributes most strongly to the increased Pr. Therefore, the two cases with and without BL horizontal advection both demonstrate tight links between rainfall and

590   convective mass flux, which is in balance with surface enthalpy fluxes through BLQE. Furthermore, surface enthalpy fluxes are substantially modulated by surface horizontal winds, which are intimately linked to the large-scale circulation in our case.

6   Conclusions

Over decades general circulation models have shown disagreement on tropical rainfall distributions, demonstrating a high level of uncertainty. Idealized modeling frameworks, such as aquaplanet simulations, showed a high sensitivity of tropical rainfall to

595   various factors. This study presented a novel diagnostic tool to disentangle the processes important for rainfall in a fully coupled and physically consistent way. The innovation of our diagnostics is the application of the conceptual framework by Emanuel (2019) to output from a numerical model. Amongst other things, the framework assumes mass and energy conservation and the boundary-layer quasi-equilibrium (BLQE) approach (Raymond, 1995). BLQE describes the balance of moist static energy in the BL between surface enthalpy fluxes and vertical advection through convective downdrafts and large-scale subsidence.
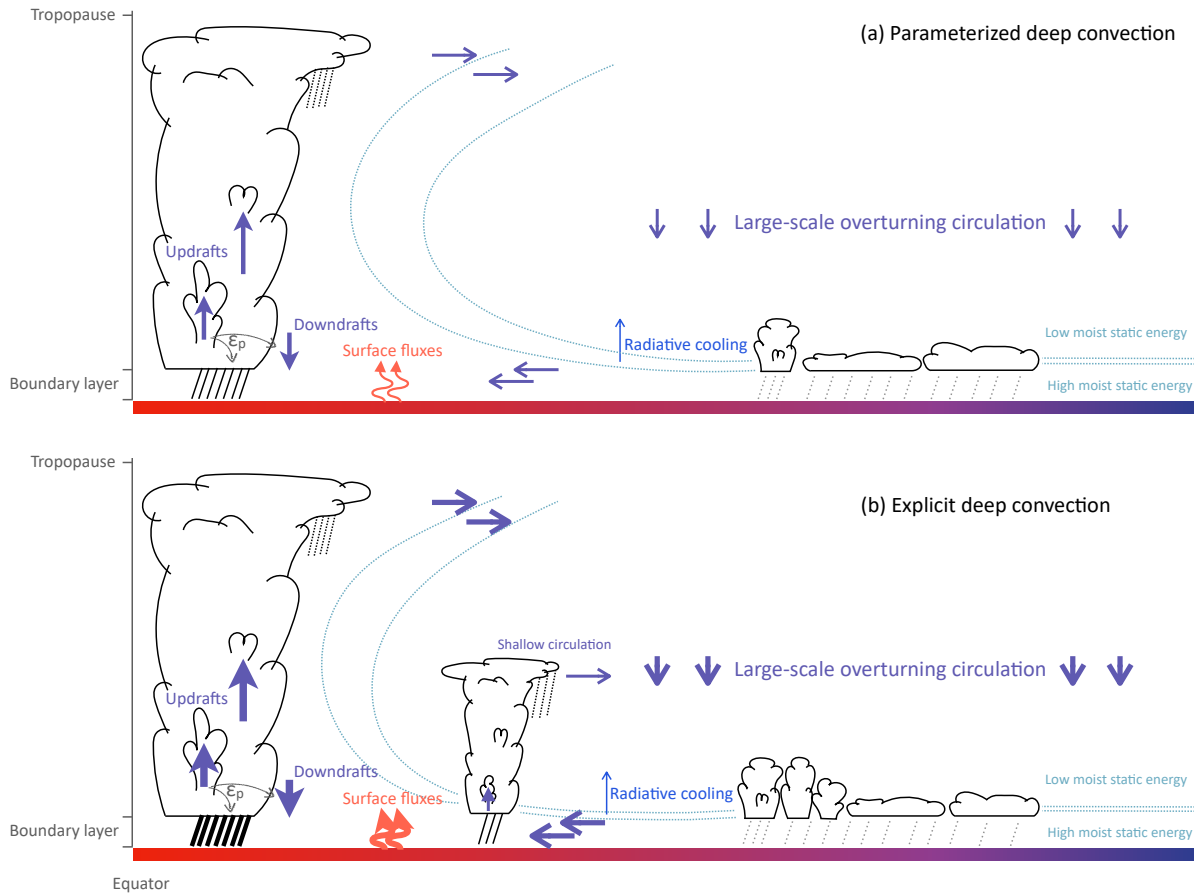
Figure 11. Schematic depiction of the important processes associated with rainfall for (a) parameterized deep convection and (b) explicit deep convection. The thick (thin) arrows and lines indicate large (small) quantities. The dotted curves indicate contour lines for constant values of moist static energy. See Sect. 6 for a detailed discussion.

600   We applied our diagnostics to tropical aquachannel experiments with different treatments of shallow and deep convection in the ICON-NWP model. The channel geometry is designed with a zonal extension as large as the Earth's circumference and a meridional extension between 30°N/S where which time-invariant, zonally constant variables are prescribed. The horizontal grid resolution is 13 km. The SSTs are prescribed with a zonally symmetric distribution and maximum at the equator (Neale and Hoskins, 2000). The experiments comprised (a) P13 with parameterized deep and shallow convection (Bechtold et al., 2008; Tiedtke, 1989), (b) S13 with explicit deep convection and parameterized shallow convection, (c) SS13 with explicit deep convection and stochastic shallow convection (Sakradzija et al., 2015, 2020) and (d) E13 with explicit deep and shallow convection.

25

All four experiments show an ITCZ at the equator and a Hadley circulation with an ascending branch at the equator and descending branches at 15°N/S – somewhat narrower than the Hadley circulation in reality – and accompanying easterly trade
610 winds at the flanks of the ITCZ. The narrower Hadley circulation is because the model develops its own internal circulation, at least partly related to suppressed eddy fluxes at the rigid walls. Despite the similar structures among the experiments, there are differences, mainly by deep convective treatment. From parameterized to explicit deep convection, the maximum precipitation in the ITCZ increases by 35 %, and the Hadley circulation and trade winds are also strengthened.

A physically consistent diagnostics was presented to understand the differences. Our diagnostics revealed important links
615 for the differences when modifying a convective treatment. Figure 11 illustrates how variables relevant to rainfall change from parameterized to explicit deep convection. The changes can be summarized as follows:

- In the ITCZ, where the rainfall amount changes substantially, the large-scale circulation and surface horizontal winds get stronger with explicit deep convection. Strong surface winds enhance surface enthalpy fluxes by 20.2–27.7 %. The vertical difference in moist static energy between the BL and the lower troposphere is relatively small in response to
620 changing convective treatment. Somewhat surprisingly, precipitation efficiency is little sensitive to the representation of convection with almost constant values of 0.629–0.648 . In contrast, convective updraft mass flux increases by 29–37 % with explicit deep convection. The constant value of precipitation efficiency indicates that convective updraft mass flux increases proportionally to increasing convective downdraft mass flux, which is balanced by enhancing surface enthalpy fluxes to maintain BLQE. Thus, the rainfall change in response to convective treatment is due to the tight links among
625 dynamical fields, surface fluxes and convective mass flux.

- In the trade wind belt, surface enthalpy fluxes and surface horizontal winds remain stronger with explicit deep convection. However, the vertical contrast of moist static energy between the BL and the lower troposphere greatly varies, depending on representation of shallow convection. Precipitation efficiency and convective updraft mass flux sharply decrease from the ITCZ, but the former is greater with parameterized deep convection (0.306) than with explicit one (0.214), while the
630 latter shows little dependence on convective treatment. Despite this difference, the small values of precipitation efficiency and convective updraft mass flux do not change rainfall significantly from one experiment to another.

In all latitudes, a change in radiative cooling is compensated by altering dry stability, so having a very small net effect on convective mass flux. Note that radiative cooling was found to be crucial for the RCE case without a large-scale circulation (Emanuel, 2019), but this is not the case for our experiments with full physics and dynamics. Moreover, explicit deep
635 convection can produce more delicate distributions of convection, such as deep, shallow and congestus clouds, than parameterized convection but again mean rainfall is insensitive to a change in radiative cooling associated with these structures. In our case column specific humidity does not play an important role for rainfall changes. With explicit deep convection, the meridional advection of moist static energy in the BL is not negligible, leading to a slight increase of precipitation efficiency from 0.64 to 0.69. However, convective updraft mass flux still exhibits the strongest association with rainfall. A caveat of this
640 diagnostics is that the effects of entrainment and detrainment are not considered, which might be important for convective

updraft mass flux (Zipser, 2003; Möbis and Stevens, 2012). Somewhat indirectly, these effects are included in $h_\mathrm{b} - h_\mathrm{m}$ through lower-tropospheric h and in ϵ_p through indirect effects of re-evaporation.

The merit of our diagnostics lies in a fair comparison of simulations with different representations of convection to examine the processes potentially linked to rainfall. Since those processes are strongly coupled to each other, it is not trivial to disen-

645 tangle what processes are ultimately responsible for rainfall. Furthermore, explicit and parameterized convection treats vertical motion differently, so it is not fair to compare convective updraft mass flux obtained directly from the modelled vertical wind field. Thus, we emphasize that the diagnostics presented here provides a physically consistent, fair comparison between explicit and parameterized convection and helps obtain a quantitative and qualitative view on important links in the system. Lastly, this tool also has potential to specify sources of uncertainty in NWP models and to identify the reasons behind the large spread in

650 ITCZ behavior among different global climate models.

Code availability. The diagnostic tools will be provided in a GitHub repository.

Data availability. During the review process, the model output of the simulations on which the analysis is based is available here for download: https://opendata.physik.lmu.de/BwDmR3qNYbtCiqB. After the review, a permanent DOI will be assigned.

Video supplement. This manuscript includes a video supplement, which shows a series of snapshots of precipitable water (shading) and
655 rainfall rate (contour) in the tropical aquachannel simulations.

Appendix A: Emanuel (2019)'s framework

In the framework of Emanuel (2019), the large-scale vertical velocity at the top of the boundary layer (BL) w is written as

$$\rho w = M_u - M_d - \rho w_e, \tag{A1}$$

where M_u and M_d are convective upward and downward mass fluxes of water vapor in $\mathrm{kg\,m^{-2}\,s^{-1}}$, respectively, w_e the
660 environmental vertical velocity away from convection, and ρ the air density at the top of the BL. Note that Emanuel (2019) uses dimensionless mass flux and vertical velocity fields but we prefer utilizing them in physical units in order to apply the conceptual model to the simulated fields. Microphysical processes are not treated explicitly but formulated through one constant parameter, the so-called precipitation efficiency ϵ_p, which represents the fraction of all condensate that reaches the ground as precipitation. Also, ϵ_p can then be used to parameterize M_d as a function of M_u in the following way: $M_d = (1 - \epsilon_p)M_u$. For
665 $\epsilon_p = 1$, all condensate precipitates, such that there is no evaporation and thus no downdraft mass flux. For $\epsilon_p = 0$, all condensate eventually evaporates again such that downdraft and updraft mass fluxes balance.

With conservation of moist static energy, h budget for the BL becomes:

$$\int_b \Big(\rho\frac{\partial h}{\partial t} + \rho \boldsymbol{V}\cdot\nabla h\Big)dz = F_{\mathrm{h}} - \int_b \dot{Q}dz, \tag{A2}$$

where $\boldsymbol{V}$ is the 3-dimensional wind velocity, F_{h} the surface enthalpy flux, $\dot{Q}$ the radiative cooling and the subscription b indicates the integral over the depth of the BL. In a well-mixed BL the vertical advection of h occurs at the top of the BL, and boundary-layer quasi-equilibrium (BLQE) assumes that the injection of low-h air by convective downdrafts (M_d) and large-scale subsidence (w_e) is balanced by the uptake of high h through surface fluxes (Raymond, 1995). Therefore, the vertical advection can be represented by a simple difference between characteristic values of h for the BL (h_{b}) and the free troposphere (h_{m}), here denoted by $h_{\mathrm{b}} - h_{\mathrm{m}}$. In quasi-equilibrium, the local time derivative vanishes and Eq. A2 becomes

$$\mathrm{d}\rho\boldsymbol{V}_h\cdot\nabla h = F_{\mathrm{h}} - \mathrm{d}\dot{Q}_b - (M_d + \rho w_e)(h_{\mathrm{b}} - h_{\mathrm{m}}), \tag{A3}$$

where d is the BL height, $\boldsymbol{V}_h$ is the horizontal velocity and $\dot{Q}_b$ is the radiative cooling at the top of the BL, which is assumed to be characteristic for the entire BL, .i.e., constant. In addition, advection is assumed to be approximately constant throughout the BL. Assuming that d is small, net radiative cooling at the top of the BL and the horizontal advection of h will be small and can be neglected. Then, Eq. A3 becomes

$$0 = F_{\mathrm{h}} - (M_d + \rho w_e)(h_{\mathrm{b}} - h_{\mathrm{m}}). \tag{A4}$$

The weak temperature gradient approximation implies that horizontal advection in the thermodynamic equation can be neglected, and time changes also vanish in quasi-equilibrium or steady state, such that thermodynamic balance is between vertical advection and diabatic heating (Sobel et al., 2001). In an ascending region, condensational heating is balanced by adiabatic cooling by an ascending parcel. In a descending region, of which the area fraction is far larger than an ascending region, adiabatic warming by subsidence is balanced by radiative cooling. The thermodynamic balance in the descending region can be formulated as as $\rho w_e S = \dot{Q}$, where $S \equiv c_p \frac{dT}{dz} + g$ is closely related to dry static stability with g the gravitational acceleration. Using Eq. A1, this can be further written as

$$(\epsilon_p M_u - \rho w) = \frac{\dot{Q}}{S}, \tag{A5}$$

which illustrates the limitation of convection by longwave cooling in the environment.

Using Eqs. A1, A4 and A5, we can then derive a diagnostic expression for M_u as

$$M_u = \frac{1}{1-\epsilon_p}\Big(\frac{F_{\mathrm{h}}}{h_{\mathrm{b}} - h_{\mathrm{m}}} - \frac{\dot{Q}}{S}\Big). \tag{A6}$$

The above formulation of M_u is employed by the ITCZ diagnostics presented in Sect. 4.

695

700

References

Arnold, N. P. and Randall, D. A.: Global-scale convective aggregation: Implications for the Madden-Julian Oscillation, J. Adv. Model. Earth Syst., 7, 1499–1518, https://doi.org/10.1002/2015MS000498, 2015.

Bechtold, P.: Atmospheric moist convection, Meteorological Training Course Lecture Series, ECMWF, 2017.

705 Bechtold, P., Köhler, M., Jung, T., Doblas-Reyes, F., Leutbecher, M., Rodwell, M. J., Vitart, F., and Balsamo, G.: Advances in simulating atmospheric variability with the ECMWF model: From synoptic to decadal time-scales, Quart. J. Roy. Met. Soc., 134, 1337–1351, https://doi.org/10.1002/qj.289, 2008.

Becker, T., Bechtold, P., and Sandu, I.: Characteristics of convective precipitation over tropical Africa in storm-resolving global simulations, Quart. J. Roy. Met. Soc., https://doi.org/10.1002/qj.4185, 2021.

710 Benedict, J. J., Medeiros, B., Clement, A. C., and Pendergrass, A. G.: Sensitivities of the hydrologic cycle to model physics, grid resolution, and ocean type in the aquaplanet Community Atmosphere Model, J. Adv. Model. Earth Syst., 9, 1307–1324, https://doi.org/10.1002/2016MS000891, 2017.

Bony, S., Stevens, B., Frierson, D. M., Jakob, C., Kageyama, M., Pincus, R., Shepherd, T. G., Sherwood, S. C., Siebesma, A. P., Sobel, A. H., et al.: Clouds, circulation and climate sensitivity, Nat. Geosci., 8, 261–268, https://doi.org/10.1038/ngeo2398, 2015.

715 Bretherton, C. S. and Khairoutdinov, M. F.: Convective self-aggregation feedbacks in near-global cloud-resolving simulations of an aquaplanet, J. Adv. Model. Earth Syst., 7, 1765–1787, https://doi.org/10.1002/2015MS000499, 2015.

Bretherton, C. S., Peters, M. E., and Back, L. E.: Relationships between water vapor path and precipitation over the tropical oceans, J. Climate, 17, 1517–1528, https://doi.org/10.1175/1520-0442(2004)017<1517:RBWVPA>2.0.CO;2, 2004.

Bretherton, C. S., Blossey, P. N., and Khairoutdinov, M.: An energy-balance analysis of deep convective self-aggregation above uniform 720 SST, J. Atmos. Sci., 62, 4273–4292, https://doi.org/10.1175/JAS3614.1, 2005.

Chan, S. C., Kendon, E. J., Fowler, H. J., Blenkinsop, S., Roberts, N. M., and Ferro, C. A.: The value of high-resolution Met Office regional climate models in the simulation of multihourly precipitation extremes, J. Climate, 27, 6155–6174, https://doi.org/10.1175/JCLI-D-13-00723.1, 2014.

Craig, G. C. and Cohen, B. G.: Fluctuations in an equilibrium convective ensemble. Part I: Theoretical formulation, J. Atmos. Sci., 63, 725 1996–2004, https://doi.org/10.1175/JAS3709.1, 2006.

Emanuel, K.: Inferences from simple models of slow, convectively coupled processes, J. Atmos. Sci., 76, 195–208, https://doi.org/10.1175/JAS-D-18-0090.1, 2019.

Emanuel, K. A., David Neelin, J., and Bretherton, C. S.: On large-scale circulations in convecting atmospheres, Quart. J. Roy. Met. Soc., 120, 1111–1143, https://doi.org/10.1002/qj.49712051902, 1994a.

730 Emanuel, K. A. et al.: Atmospheric convection, Oxford University Press on Demand, 1994b.

Fiedler, S., Crueger, T., D'Agostino, R., Peters, K., Becker, T., Leutwyler, D., Paccini, L., Burdanowitz, J., Buehler, S. A., Cortes, A. U., et al.: Simulated tropical precipitation assessed across three major phases of the coupled model intercomparison project (CMIP), Mon. Wea. Rev., 148, 3653–3680, https://doi.org/10.1175/MWR-D-19-0404.1, 2020.

Gehne, M., Wolding, B., Dias, J., and Kiladis, G. N.: Diagnostics of tropical variability for numerical weather forecasts, Weather and Fore-735 casting, 37, 1661–1680, https://doi.org/10.1175/WAF-D-21-0204.1, 2022.

Giorgi, F.: Sensitivity of simulated summertime precipitation over the western United States to different physics parameterizations, Mon. Wea. Rev., 119, 2870–2888, https://doi.org/10.1175/1520-0493(1991)119<2870:SOSSPO>2.0.CO;2, 1991.

Hartmann, D. L. and Michelsen, M. L.: No evidence for iris, Bull. Am. Met. Soc., 83, 249–254, https://doi.org/10.1175/1520-0477(2002)083<0249:NEFI>2.3.CO;2, 2002.

740   Hong, S.-Y. and Dudhia, J.: Next-generation numerical weather prediction: Bridging parameterization, explicit clouds, and large eddies, Bull. Am. Met. Soc., 93, ES6–ES9, https://doi.org/10.1175/2011BAMS3224.1, 2012.

Hsu, C.-W., DeMott, C. A., Branson, M., Reeves Eyre, J., and Zeng, X.: Ocean Surface Flux Algorithm Effects on Tropical Indo-Pacific Intraseasonal Precipitation, Geophys. Res. Lett., 49, e2021GL096 968, https://doi.org/10.1029/2021GL096968, 2022.

Jeevanjee, N.: Vertical velocity in the gray zone, J. Adv. Model. Earth Syst., 9, 2304–2316, https://doi.org/10.1002/2017MS001059, 2017.

745   Johnson, R. H., Rickenbach, T. M., Rutledge, S. A., Ciesielski, P. E., and Schubert, W. H.: Trimodal characteristics of tropical convection, J. Climate, 12, 2397–2418, https://doi.org/10.1175/1520-0442(1999)012<2397:TCOTC>2.0.CO;2, 1999.

Judt, F. and Rios-Berrios, R.: Resolved Convection Improves the Representation of Equatorial Waves and Tropical Rainfall Variability in a Global Nonhydrostatic Model, Geophys. Res. Lett., 48, e2021GL093 265, https://doi.org/10.1029/2021GL093265, 2021.

Jung, H. and Knippertz, P.: Link between the time-space behavior of rainfall and 3D dynamical structures of equatorial waves in global
750   convection-permitting simulations, Geophys. Res. Lett., 50, e2022GL100 973, https://doi.org/10.1029/2022GL100973, 2023.

Khairoutdinov, M. F. and Emanuel, K.: Intraseasonal variability in a cloud-permitting near-global equatorial aquaplanet model, J. Atmos. Sci., 75, 4337–4355, https://doi.org/10.1175/JAS-D-18-0152.1, 2018.

Khairoutdinov, M. F., Krueger, S. K., Moeng, C.-H., Bogenschutz, P. A., and Randall, D. A.: Large-eddy simulation of maritime deep tropical convection, J. Adv. Model. Earth Syst., 1, https://doi.org/10.3894/JAMES.2009.1.15, 2009.

755   Kwon, Y. C. and Hong, S.-Y.: A mass-flux cumulus parameterization scheme across gray-zone resolutions, Mon. Wea. Rev., 145, 583–598, https://doi.org/10.1175/MWR-D-16-0034.1, 2017.

Landu, K., Leung, L. R., Hagos, S., Vinoj, V., Rauscher, S. A., Ringler, T., and Taylor, M.: The dependence of ITCZ structure on model resolution and dynamical core in aquaplanet simulations, J. Climate, 27, 2375–2385, https://doi.org/10.1175/JCLI-D-13-00269.1, 2014.

Lau, W. K., Kim, K.-M., Chern, J.-D., Tao, W.-K., and Leung, L. R.: Structural changes and variability of the ITCZ induced by
760   radiation–cloud–convection–circulation interactions: inferences from the Goddard Multi-scale Modeling Framework (GMMF) experiments, Clim. Dynam., 54, 211–229, https://doi.org/10.1007/s00382-019-05000-y, 2020.

Li, F., Collins, W. D., Wehner, M. F., Williamson, D. L., Olson, J. G., and Algieri, C.: Impact of horizontal resolution on simulation of precipitation extremes in an aqua-planet version of Community Atmospheric Model (CAM3), TELLUS A, 63, 884–892, https://doi.org/10.1111/j.1600-0870.2011.00544.x, 2011.

765   Lindzen, R. S., Chou, M.-D., and Hou, A. Y.: Does the earth have an adaptive infrared iris?, Bull. Am. Met. Soc., 82, 417–432, https://doi.org/10.1175/1520-0477(2001)082<0417:DTEHAA>2.3.CO;2, 2001.

Marsham, J. H., Dixon, N. S., Garcia-Carreras, L., Lister, G. M., Parker, D. J., Knippertz, P., and Birch, C. E.: The role of moist convection in the West African monsoon system: Insights from continental-scale convection-permitting simulations, Geophys. Res. Lett., 40, 1843–1849, https://doi.org/10.1002/grl.50347, 2013.

770   Mauritsen, T. and Stevens, B.: Missing iris effect as a possible cause of muted hydrological change and high climate sensitivity in models, Nat. Geosci., 8, 346–351, https://doi.org/10.1038/ngeo2414, 2015.

Medeiros, B., Williamson, D. L., and Olson, J. G.: Reference aquaplanet climate in the Community Atmosphere Model, Version 5, J. Adv. Model. Earth Syst., 8, 406–424, https://doi.org/10.1002/2015MS000593, 2016.

Mellor, G. L. and Yamada, T.: Development of a turbulence closure model for geophysical fluid problems, Rev. Geophys., 20, 851–875,
775   https://doi.org/10.1029/RG020i004p00851, 1982.

Mlawer, E. J., Taubman, S. J., Brown, P. D., Iacono, M. J., and Clough, S. A.: Radiative transfer for inhomogeneous atmospheres: RRTM, a validated correlated-k model for the longwave, J. Geophys. Res. Atmos., 102, 16 663–16 682, https://doi.org/10.1029/97JD00237, 1997.

Möbis, B. and Stevens, B.: Factors controlling the position of the Intertropical Convergence Zone on an aquaplanet, J. Adv. Model. Earth Syst., 4, https://doi.org/10.1029/2012MS000199, 2012.

780 Muller, C. and Takayabu, Y.: Response of precipitation extremes to warming: what have we learned from theory and idealized cloud-resolving simulations, and what remains to be learned?, Environ. Res. Lett., 15, 035 001, https://doi.org/10.1088/1748-9326/ab7130, 2020.

Narsey, S., Jakob, C., Singh, M. S., Bergemann, M., Louf, V., Protat, A., and Williams, C.: Convective precipitation efficiency observed in the tropics, Geophys. Res. Lett., 46, 13 574–13 583, https://doi.org/10.1029/2019GL085031, 2019.

Naumann, A. K., Stevens, B., and Hohenegger, C.: A moist conceptual model for the boundary layer structure and radiatively driven shallow circulations in the trades, J. Atmos. Sci., 76, 1289–1306, https://doi.org/10.1175/JAS-D-18-0226.1, 2019.

Neale, R. B. and Hoskins, B. J.: A standard test for AGCMs including their physical parametrizations: I: The proposal, Atmos. Sci. Let., 1, 101–107, https://doi.org/10.1006/asle.2000.0022, 2000.

Nolan, D. S., Tulich, S. N., and Blanco, J. E.: ITCZ structure as determined by parameterized versus explicit convection in aquachannel and aquapatch simulations, J. Adv. Model. Earth Syst., 8, 425–452, https://doi.org/10.1002/2015MS000560, 2016.

790 Paccini, L., Hohenegger, C., and Stevens, B.: Explicit versus parameterized convection in response to the Atlantic Meridional Mode, J. Climate, 34, 3343–3354, https://doi.org/10.1175/JCLI-D-20-0224.1, 2021.

Palmer, T. and Stevens, B.: The scientific challenge of understanding and estimating climate change, Proc. Natl. Acad. Sci., 116, 24 390–24 395, https://doi.org/10.1073/pnas.1906691116, 2019.

Pante, G. and Knippertz, P.: Resolving Sahelian thunderstorms improves mid-latitude weather forecasts, Nat. Commun., 10, 3487, https://doi.org/10.1038/s41467-019-11081-4, 2019.

795 Prein, A. F., Langhans, W., Fosser, G., Ferrone, A., Ban, N., Goergen, K., Keller, M., Tölle, M., Gutjahr, O., Feser, F., et al.: A review on regional convection-permitting climate modeling: Demonstrations, prospects, and challenges, Rev. Geophys., 53, 323–361, https://doi.org/10.1002/2014RG000475, 2015.

Rajendran, K., Kitoh, A., and Srinivasan, J.: Effect of SST variation on ITCZ in APE simulations, J. Met. Soc. Jap., 91, 195–215, https://doi.org/10.2151/jmsj.2013-A06, 2013.

800 Randall, D. A.: Beyond deadlock, Geophys. Res. Lett., 40, 5970–5976, https://doi.org/10.1002/2013GL057998, 2013.

Raschendorfer, M.: The new turbulence parameterization of LM, COSMO newsletter, 1, 89–97, 2001.

Raymond, D., Fuchs, Ž., Gjorgjievska, S., and Sessions, S.: Balanced dynamics and convection in the tropical troposphere, J. Adv. Model. Earth Syst., 7, 1093–1116, https://doi.org/10.1002/2015MS000467, 2015.

805 Raymond, D. J.: Regulation of moist convection over the west Pacific warm pool, J. Atmos. Sci., 52, 3945–3959, https://doi.org/10.1175/1520-0469(1995)052<3945:ROMCOT>2.0.CO;2, 1995.

Raymond, D. J., Bretherton, C. S., and Molinari, J.: Dynamics of the intertropical convergence zone of the east Pacific, J. Atmos. Sci., 63, 582–597, https://doi.org/10.1175/JAS3642.1, 2006.

Retsch, M.-H., Hohenegger, C., and Stevens, B.: Vertical resolution refinement in an aqua-planet and its effect on the ITCZ, 810 J. Adv. Model. Earth Syst., 9, 2425–2436, https://doi.org/10.1002/2017MS001010, 2017.

Retsch, M. H., Mauritsen, T., and Hohenegger, C.: Climate change feedbacks in aquaplanet experiments with explicit and parametrized convection for horizontal resolutions of 2,525 up to 5 km, J. Adv. Model. Earth Syst., 11, 2070–2088, https://doi.org/10.1029/2019MS001677, 2019.

Rios-Berrios, R., Medeiros, B., and Bryan, G.: Mean Climate and Tropical Rainfall Variability in Aquaplanet Simulations Using the Model
for Prediction Across Scales-Atmosphere, J. Adv. Model. Earth Syst., 12, e2020MS002 102, https://doi.org/10.1029/2020MS002102,
2020.

Rios-Berrios, R., Bryan, G. H., Medeiros, B., Judt, F., and Wang, W.: Differences in Tropical Rainfall in Aquaplanet Simulations With
Resolved or Parameterized Deep Convection, J. Adv. Model. Earth Syst., p. e2021MS002902, https://doi.org/10.1029/2021MS002902,
2022.

Sakradzija, M. and Hohenegger, C.: What determines the distribution of shallow convective mass flux through a cloud base?, J. Atmos. Sci.,
74, 2615–2632, https://doi.org/10.1175/JAS-D-16-0326.1, 2017.

Sakradzija, M., Seifert, A., and Heus, T.: Fluctuations in a quasi-stationary shallow cumulus cloud ensemble, Nonlinear Processes Geophys.,
22, 65–85, https://doi.org/https://doi:10.5194/npg-22-65-2015, 2015.

Sakradzija, M., Senf, F., Scheck, L., Ahlgrimm, M., and Klocke, D.: Local impact of stochastic shallow convection on clouds and precipitation
in the tropical Atlantic, Mon. Wea. Rev., 148, 5041–5062, https://doi.org/10.1175/MWR-D-20-0107.1, 2020.

Satoh, M., Tomita, H., Yashiro, H., Kajikawa, Y., Miyamoto, Y., Yamaura, T., Miyakawa, T., Nakano, M., Kodama, C., Noda, A. T., Nasuno,
T., Yamada, Y., and Fukutomi, Y.: Outcomes and challenges of global high-resolution non-hydrostatic atmospheric simulations using the
K computer, Prog Earth Planet Sci., 4, 1–24, https://doi.org/10.1186/s40645-017-0127-8, 2017.

Schär, C., Fuhrer, O., Arteaga, A., Ban, N., Charpilloz, C., Di Girolamo, S., Hentgen, L., Hoefler, T., Lapillonne, X., Leutwyler, D., et al.:
Kilometer-scale climate models: Prospects and challenges, Bull. Am. Met. Soc., 101, E567–E587, https://doi.org/10.1175/BAMS-D-18-
0167.1, 2020.

Schlemmer, L., Bechtold, P., Sandu, I., and Ahlgrimm, M.: Uncertainties related to the representation of momentum transport in shallow
convection, J. Adv. Model. Earth Syst., 9, 1269–1291, https://doi.org/10.1002/2017MS000915, 2017.

Schneider, T., Bischoff, T., and Haug, G. H.: Migrations and dynamics of the intertropical convergence zone, NATURE, 513, 45–53,
https://doi.org/10.1038/nature13636, 2014.

Schwendike, J., Govekar, P., Reeder, M. J., Wardle, R., Berry, G. J., and Jakob, C.: Local partitioning of the overturning cir-
culation in the tropics and the connection to the Hadley and Walker circulations, J. Geophys. Res. Atmos., 119, 1322–1339,
https://doi.org/10.1002/2013JD020742, 2014.

Scinocca, J. F. and McFarlane, N. A.: The variability of modeled tropical precipitation, J. Atmos. Sci., 61, 1993–2015,
https://doi.org/10.1175/1520-0469(2004)061<1993:TVOMTP>2.0.CO;2, 2004.

Seifert, A.: A revised cloud microphysical parameterization for COSMO-LME, COSMO Newsletter, 7, 25–28, 2008.

Senf, F., Voigt, A., Clerbaux, N., Hünerbein, A., and Deneke, H.: Increasing Resolution and Resolving Convection Improve the Simulation of
Cloud-Radiative Effects Over the North Atlantic, J. Geophys. Res. Atmos., 125, e2020JD032 667, https://doi.org/10.1029/2020JD032667,
2020.

Sobel, A. H., Nilsson, J., and Polvani, L. M.: The weak temperature gradient approximation and balanced tropical moisture waves, J. At-
mos. Sci., 58, 3650–3665, https://doi.org/10.1175/1520-0469(2001)058<3650:TWTGAA>2.0.CO;2, 2001.

Stephan, C. C., Strube, C., Klocke, D., Ern, M., Hoffmann, L., Preusse, P., and Schmidt, H.: Gravity waves in global high-resolution sim-
ulations with explicit and parameterized convection, J. Geophys. Res. Atmos., 124, 4446–4459, https://doi.org/10.1029/2018JD030073,
2019.

Stephens, G. L.: Cloud feedbacks in the climate system: A critical review, J. Climate, 18, 237–273, https://doi.org/10.1175/JCLI-3243.1,
2005.

Stevens, B. and Bony, S.: What are climate models missing?, Science, 340, 1053–1054, https://doi.org/10.1126/science.1237554, 2013.

Stevens, B., Satoh, M., Auger, L., Biercamp, J., Bretherton, C. S., Chen, X., Düben, P., Judt, F., Khairoutdinov, M., Klocke, D., Kodama, C., Kornblueh, L., Lin, S.-J., Neumann, P., Putman, W. M., Röber, N., Shibuya, R., Vanniere, B., Vidale, P. L., Wedi, N., and Linjiong, Z.:

855   DYAMOND: The DYnamics of the atmospheric general circulation modeled on non-hydrostatic domains, Prog Earth Planet Sci., 6, 61, https://doi.org/10.1186/s40645-019-0304-z, 2019.

Stevens, B., Acquistapace, C., Hansen, A., Heinze, R., Klinger, C., Klocke, D., Rybka, H., Schubotz, W., Windmiller, J., Adamidis, P., et al.: The added value of large-eddy and storm-resolving models for simulating clouds and precipitation, J. Met. Soc. Jap., 98, 395–435, https://doi.org/10.2151/jmsj.2020-021, 2020.

860 Tian, B. and Dong, X.: The double-ITCZ bias in CMIP3, CMIP5, and CMIP6 models based on annual mean precipitation, Geophys. Res. Lett., 47, e2020GL087 232, https://doi.org/10.1029/2020GL087232, 2020.

Tiedtke, M.: A comprehensive mass flux scheme for cumulus parameterization in large-scale models, Mon. Wea. Rev., 117, 1779–1800, https://doi.org/10.1175/1520-0493(1989)117<1779:ACMFSF>2.0.CO;2, 1989.

Tomassini, L.: The interaction between moist convection and the atmospheric circulation in the tropics, Bull. Am. Met. Soc., 101, E1378–

865   E1396, https://doi.org/10.1175/BAMS-D-19-0180.1, 2020.

Webster, P. J.: Dynamics of the Tropical Atmosphere and Oceans, Wiley-Blackwell, 2020.

Wedi, N. P., Polichtchouk, I., Dueben, P., Anantharaj, V. G., Bauer, P., Boussetta, S., Browne, P., Deconinck, W., Gaudin, W., Hadade, I., Hatfield, S., Iffrig, O., Lopez, P., Maciel, P., Mueller, A., Saarinen, S., Sandu, I., Quintino, T., and Vitart, F.: A baseline for global weather and climate simulations at 1 km resolution, J. Adv. Model. Earth Syst., 12, e2020MS002 192, https://doi.org/10.1029/2020MS002192,

870   2020.

Weisman, M. L., Skamarock, W. C., and Klemp, J. B.: The resolution dependence of explicitly modeled convective systems, Mon. Wea. Rev., 125, 527–548, https://doi.org/10.1175/1520-0493(1997)125<0527:TRDOEM>2.0.CO;2, 1997.

Zängl, G., Reinert, D., Rípodas, P., and Baldauf, M.: The ICON (ICOsahedral Non-hydrostatic) modelling framework of DWD and MPI-M: Description of the non-hydrostatic dynamical core, Quart. J. Roy. Met. Soc., 141, 563–579, https://doi.org/10.1002/qj.2378, 2015.

875 Zipser, E. J.: Some views on "hot towers" after 50 years of tropical field programs and two years of TRMM data, in: Cloud Systems, Hurricanes, and the Tropical Rainfall Measuring Mission (TRMM), edited by Tao, W.-K. and Adler, R., pp. 49–58, Springer, https://doi.org/10.1007/978-1-878220-63-9_5, 2003.